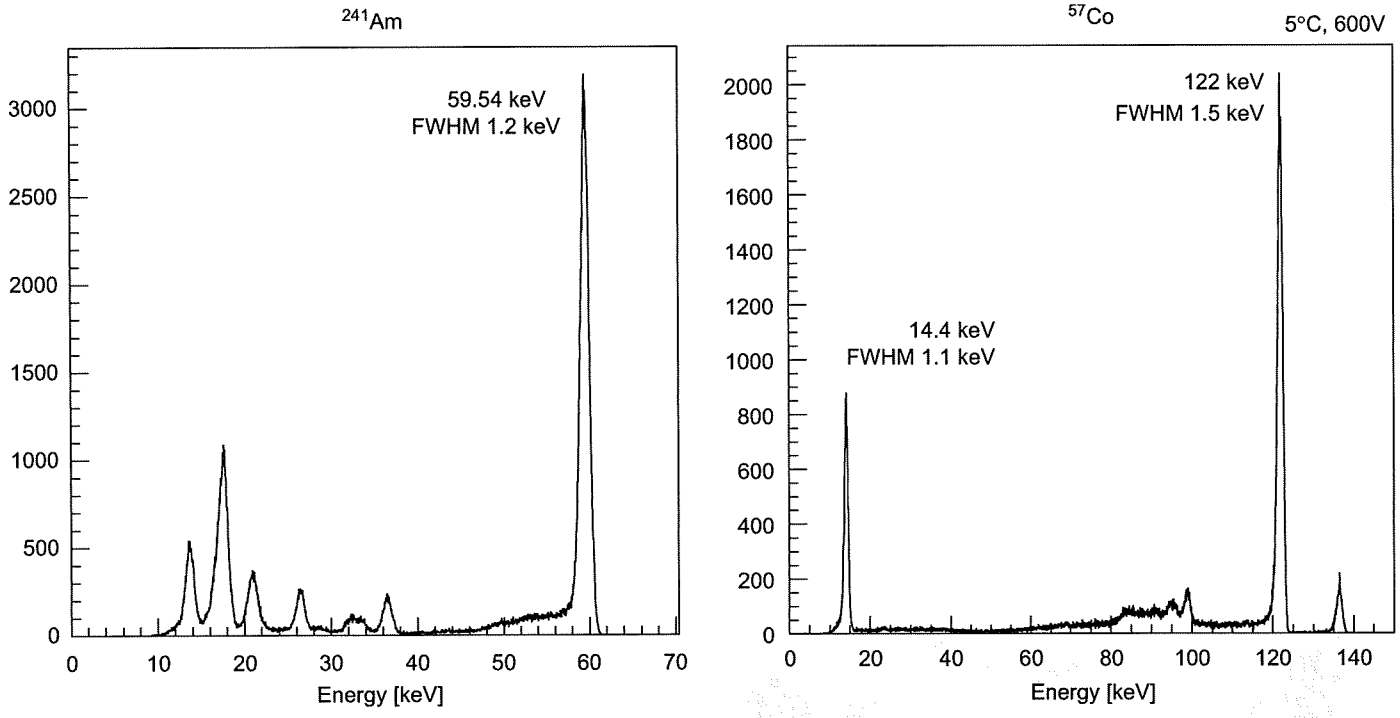

Fig. 7. The ^{241}Am and ^{57}Co spectra obtained from one of the CdTe pixel detector modules. These are summed spectra from all 64 pixels. The applied bias voltage is 600 V, and, the operating temperature is 5 °C. The energy resolutions are 1.2 and 1.5 keV (FWHM) at 59.5 and 122 keV, respectively.

modules. For 64 spectra from all pixels, gain corrections were performed and then all corrected spectra were summed. The applied bias voltage was 600 V and the operating temperature was 5 °C. The energy resolutions were 1.2 and 1.5 keV (FWHM) at 59.5 and 122 keV, respectively. The remarkably close resolution results were achieved for all the pixel modules, using the 74 CdTe devices selected from the leakage current measurement tests mentioned above.

5. CdTe stack detector as the absorber detector for the Compton camera

Stacking a number of thin CdTe detectors is a good way to obtain a high detection efficiency for higher energy gamma-rays. Since the carriers in CdTe have low mobility and a short life time, it is difficult for thick CdTe devices to accomplish full charge collections and high energy resolution. In our previous studies, we demonstrated that both good energy resolution and good detection efficiency can be achieved with the CdTe stack detector. These were achieved using planar CdTe diode detectors with a thickness of 0.5 mm [16–18]. As the absorber detector of the Compton camera, three-dimensional position detection capabilities are necessary in addition to good energy resolution and good detection efficiency. Therefore, in order to build a good absorber detector, we have constructed a CdTe pixel stack detector by stacking the CdTe pixel detector modules.

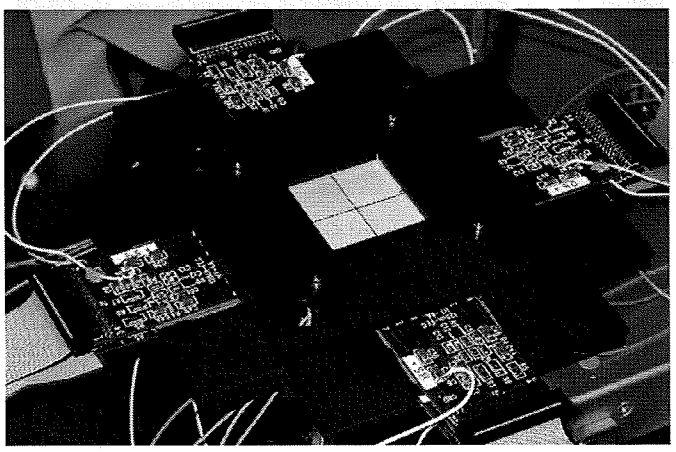

Fig. 8. The CdTe stack detector. Four layers are stacked. The stack pitch is 2 mm. A layer consists of $2 \times 2 = 4$ CdTe pixel modules.

Fig. 8 shows the stack detector. It has four layers with each layer consisting of the $2 \times 2 = 4$ pixel modules. A stack pitch between layers of 2 mm was attained in this detector.

In order to test performance as an absorber detector, we performed experiments using gamma-rays from radio isotopes. Fig. 9 shows obtained spectra of gamma-rays from ^{133}Ba. Photo-electric absorption peaks are clearly seen in the spectra. The gray lines show the spectra from the first, the second, the third and the fourth layer, respectively. On the low energy side, only the first layer detects gamma-rays. On the other hand, the peak areas

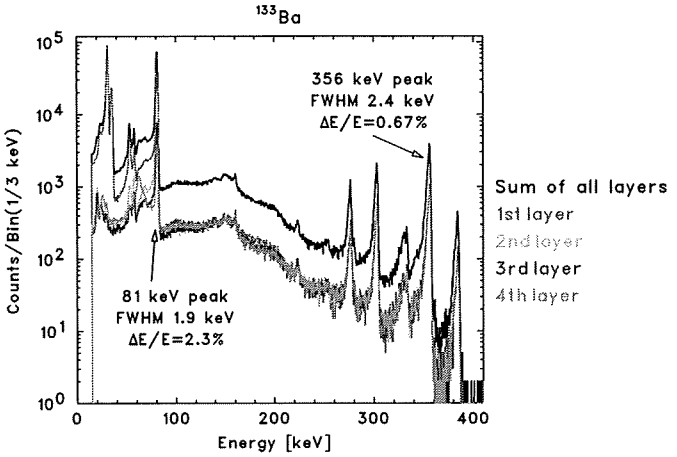

Fig. 9. ^{133}Ba spectra obtained with the CdTe stack detector. The spectrum from each layer is shown in gray, and the summed spectrum of all layers is shown in black. The energy resolutions (FWHM) achieved are 1.9 and 2.4 keV at 81 and 356 keV, respectively.

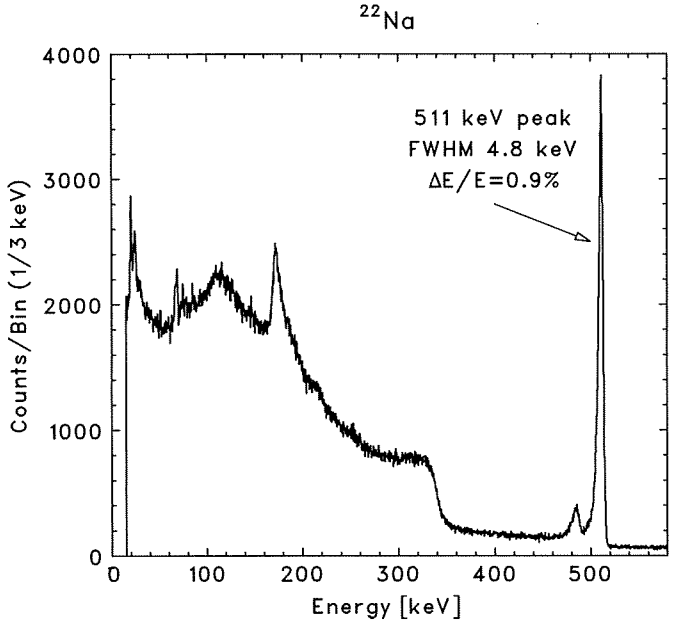

Fig. 10. A 511 keV gamma-ray spectrum obtained with the CdTe stack detector. A ^{22}Na radioisotope is used. The FWHM for 511 keV gamma-ray peak is 4.8 keV ($\Delta E/E$~0.9%).

detected in all layers are almost identical. This shows that the detection efficiency for higher energy gamma-rays was improved by stacking detectors. A 511 keV gamma-ray spectrum obtained with the CdTe stack detector is shown in Fig. 10. The achieved energy resolution is ΔE(FWHM)/E~0.9% at an operating temperature of −20 °C and under the bias voltage of 600 V.

6. Other applications of the CdTe pixel modules

Once CdTe pixel detector modules have been established, they have a variety of applications. One example is a CdTe stack, as discussed in Section 5. This works as a gamma-ray probe with a high energy resolution.

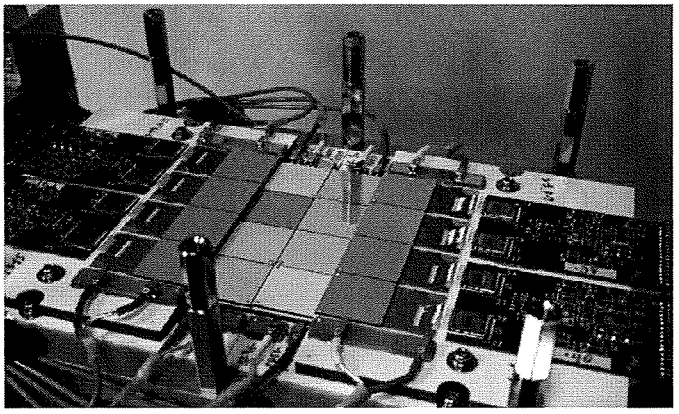

Fig. 11. The large area CdTe imager. The 4 × 4 = 16 CdTe pixel modules are arranged in plates.

Another application is as a large area CdTe imager. By arranging the modules, a CdTe imager with a large area and a high energy resolution can be created. Fig. 11 shows our constructed CdTe imager. The 4 × 4 = 16 CdTe pixel detector modules are arranged on a plate. The total size of the imager is 5.4 cm × 5.4 cm. By attaching a collimator above the image, it works as a conventional gamma camera. Because the imager has a high energy resolution (~1%), various gamma-ray lines can be easily separated in the obtained spectra. Therefore, the imager is capable of simultaneous multi tracer imaging in which different gamma-ray lines are used.

7. Conclusion

We have developed Si and CdTe imaging detectors for the Compton camera. The new four layer DSSD stack and the four layer CdTe pixel detector stack were, respectively, constructed as a scatterer detector and an absorber detector for the Compton camera. The noise performances of the stack detectors was found to be good. With the DSSD stack, we obtained an energy resolution of 1.5 keV (FWHM) for 60 keV gamma-ray photons. For the CdTe pixel detector stack, a $\Delta E/E$~1% energy resolution (FWHM) was achieved. As a next step, we will construct a new Si/CdTe Compton camera using the DSSD stack and the CdTe pixel detector stack.

Acknowledgment

The authors would like to thank C. Baluta for reading the manuscript.

References

[1] T. Takahashi, et al., SPIE 4851 (2003) 1228.
[2] T. Tanaka, et al., SPIE 5501 (2004) 229.
[3] R. Ribberfors, Phys. Rev. B 12 (1975) 2067.

[4] S. Watanabe, et al., IEEE Trans. Nucl. Sci. NS-52 (5) (2005) 2045.
[5] T. Tanaka et al., Nucl. Instr. and Meth. A 568 (2006) 375.
[6] T. Takahashi, et al., Nucl. Instr. and Meth. A 436 (2000) 111.
[7] T. Takahashi, S. Watanabe, IEEE Trans. Nucl. Sci. NS-48 (4) (2001) 950.
[8] T. Takahashi, et al., IEEE Trans. Nucl. Sci. NS-48 (3) (2001) 287.
[9] T. Takahashi, et al., New Astron. Rev. 48 (2004) 309.
[10] H. Odaka, et al., Nucl. Instr. and Meth. A (2007), doi:10.1016/j.nima.2007.05.293.
[11] S. Takeda, et al., Nucl. Instr. and Meth. A (2007), doi:10.1016/j.nima.2007.05.305.
[12] T. Tanaka, et al., New Astron. Rev. 48 (2004) 269.
[13] T. Takahashi, et al., IEEE Trans. Nucl. Sci. NS-49 (2002) 1297.
[14] K. Nakazawa, et al., IEEE Trans. Nucl. Sci. NS-51 (4) (2004) 1881.
[15] S. Watanabe, et al., Nucl. Instr. and Meth. A 567 (2006) 150.
[16] T. Takahashi, B. Paul, K. Hirose, C. Matsumoto, R. Ohno, T. Ozaki, K. Mori, Y. Tomita, Nucl. Instr. and Meth. A 436 (1999) 111.
[17] S. Watanabe, et al., IEEE Trans. Nucl. Sci. NS-49 (3) (2002) 1292.
[18] S. Watanabe, et al., Nucl. Instr. and Meth. A 505 (2003) 118.

Available online at www.sciencedirect.com
ScienceDirect
ELSEVIER
Nuclear Instruments and Methods in Physics Research A 579 (2007) 878–885
NUCLEAR INSTRUMENTS & METHODS IN PHYSICS RESEARCH Section A
www.elsevier.com/locate/nima

Performance study of Si/CdTe semiconductor Compton telescopes with Monte Carlo simulation

Hirokazu Odaka[a,b,*], Shin'ichiro Takeda[a,b], Shin Watanabe[a], Shin-nosuke Ishikawa[a,b], Masayoshi Ushio[a,b], Takaaki Tanaka[a,b], Kazuhiro Nakazawa[a], Tadayuki Takahashi[a,b], Hiroyasu Tajima[c], Yasushi Fukazawa[d]

[a]*Department of High Energy Astrophysics, Institute of Space and Astronautical Science (ISAS), Japan Aerospace Exploration Agency (JAXA), 3-1-1 Yoshinodai, Sagamihara 229-8510, Japan*
[b]*Department of Physics, Graduate School of Science, University of Tokyo, Hongo 7-3-1, Bunkyo 113-0033, Japan*
[c]*Stanford Linear Accelerator Center (SLAC), 2575 Sand Hill Road, Menlo Park, CA 94025, USA*
[d]*Department of Physical Science, Hiroshima University, 1-3-1 Kagamiyama, Higashi-Hiroshima 739-8526, Japan*

Available online 31 May 2007

Abstract

A Compton telescope with high angular resolution and high energy resolution is a promising detector for the next generation of astrophysics space missions aiming at hard X-rays and sub-MeV/MeV gamma-rays. We have been working on a semiconductor Compton camera based on silicon and cadmium telluride (Si/CdTe Compton telescope). The soft gamma-ray detector (SGD) employs a Si/CdTe Compton camera combined with a well-type active shield. It will be mounted on the NeXT mission, proposed to be launched around 2012. One Compton camera module in the SGD will consist of 24 layers of double-sided silicon strip detectors and four layers of CdTe pixel detectors. We carried out Monte Carlo simulations to investigate the basic performance of the detector. Design parameters of devices required in the simulation, such as energy resolution and position resolution of the detector, are based on the results from our prototype detector. From the simulation using current design parameters, the detection efficiency is found to be higher than 10% at ~100 keV and the angular resolution to be 9° and 4.4° at 120 keV and 330 keV, respectively. The effects of changing the design parameters are also discussed.

PACS: 95.55.Ka; 29.40.Wk

Keywords: Gamma-ray detector; Compton telescope; Monte Carlo simulation

1. Introduction

Gamma-rays in the energy range from several tens of keV to several MeV provide an important window to the study of energetic phenomena in the universe such as nucleosynthesis and particle acceleration. These phenomena are observed in objects such as pulsars, stellar black-hole candidates, supernova remnants, active galactic nuclei, and gamma-ray bursts. The observational sensitivity in this energy band, however, is relatively low due to high background levels, low detection efficiency, and limited angular resolution. Compton telescopes are promising detectors to overcome these problems since the direction of incident γ-rays is constrained by Compton kinematics, greatly reducing the background as compared with detectors which employ a coded mask or a collimator.

The first successful Compton telescope in orbit was COMPTEL aboard the Compton gamma-ray observatory (CGRO) [1]. COMPTEL observations provided pioneering results including all sky imaging from 1 to 30 MeV and spectroscopy of MeV gamma-ray lines [2]. But the number of detected objects was very small, with only 32 sources

*Corresponding author. Department of High Energy Astrophysics, Institute of Space and Astronautical Science (ISAS), Japan Aerospace Exploration Agency (JAXA), 3-1-1 Yoshinodai, Sagamihara 229-8510, Japan.
E-mail address: odaka@astro.isas.jaxa.jp (H. Odaka).

0168-9002/$ - see front matter © 2007 Published by Elsevier B.V.
doi:10.1016/j.nima.2007.05.293

detected [3]. Thus improving the sensitivity is the key goal of the next generation detectors. This requires a higher detection efficiency, a lower instrumental background and better angular resolution [4]. A high density detector array with improved energy and position resolution is needed. With this point of view, Compton telescopes based on position-sensitive semiconductor detectors, such as Si, Ge, CZT, and CdTe, have been proposed and developed by various groups [5–10].

Our group has proposed building a Si/CdTe Compton telescope based on the recent achievements of the development of Si and CdTe semiconductor imaging detectors with high energy resolution [9]. A schematic drawing of a Si/CdTe Compton telescope is shown in Fig. 1. The telescope is based on a hybrid semiconductor gamma-ray detector consisting of layers of thin Si and CdTe to detect photons in a wide energy band (0.05–1 MeV). Through using a prototype Compton camera, we succeeded in reconstructing images and spectra of gamma-rays from 81 to 662 keV. We were also able to make photon polarization measurements [11–13].

The Si/CdTe Compton telescope is adopted as one of instruments on board the NeXT (New X-ray Telescope/ Non-thermal Energy eXploration Telescope) mission, proposed in Japan as a successor to the current Suzaku X-ray mission. A detailed description of the instrument, refered to as the SGD (soft gamma-ray detector), is presented in Takahashi et al. [14]. Since the SGD must outperform previous soft γ-ray instruments in background rejection capability, the optimization of the design is of great importance. For this purpose, we have studied the performance of the Si/CdTe Compton telescope by using Monte Carlo simulations. Experimental results of the prototype Compton camera are used for assuming parameters of devices, for example, energy and position resolution of the detector. Initial results of simulations regarding the detection efficiency and performance as a polarimeter were presented in our previous publication [15]. In this paper, we present new results on the performance of the Si/CdTe detector in the SGD. In particular, the detection efficiency as a function of various design parameters and the angular resolution as a function of various data selection are described in detail.

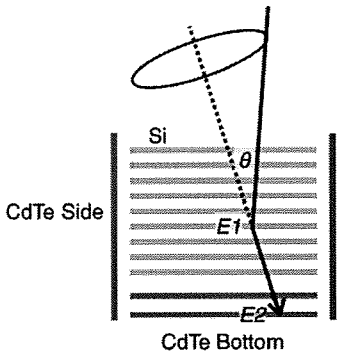

Fig. 1. Schematic picture of a Si/CdTe Compton camera. An incident photon is scattered at a silicon detector and then absorbed at a CdTe detector. E_1 and E_2 are energy deposited of the two hits, and θ is the scatter angle.

2. Simulation Setup

Fig. 2 shows a schematic diagram of the geometry of the detector used in the simulation. The telescope consists of 24 layers of double-sided silicon strip detectors (DSSDs) and four layers of thin CdTe pixellated detectors (CdTe Bottom) with a thickness of 0.5 mm. The sides are also surrounded by CdTe pixel detectors (CdTe Side). In order to lower the background dramatically and thus to improve the sensitivity, we combine a stack of Si strip detectors and CdTe pixel detectors to form a Compton telescope. This configuration is suitable for a Compton camera, since Si has a small cross-section for photo absorption even for very soft γ-rays (e.g. ~80 keV) and CdTe has a large cross-section for photo absorption due to their large atomic numbers ($Z_{Cd} = 48$, $Z_{Te} = 52$). The telescope is then mounted inside the bottom of a well-type active shield to further reduce the background by adopting a new concept, narrow-Field-of-View (FOV) Compton telescope [14,16].

The size of an individual DSSD is 50 mm × 50 mm with a thickness of 0.5 mm, and each DSSD has 125 strips on each side with a strip pitch of 0.4 mm. The energy

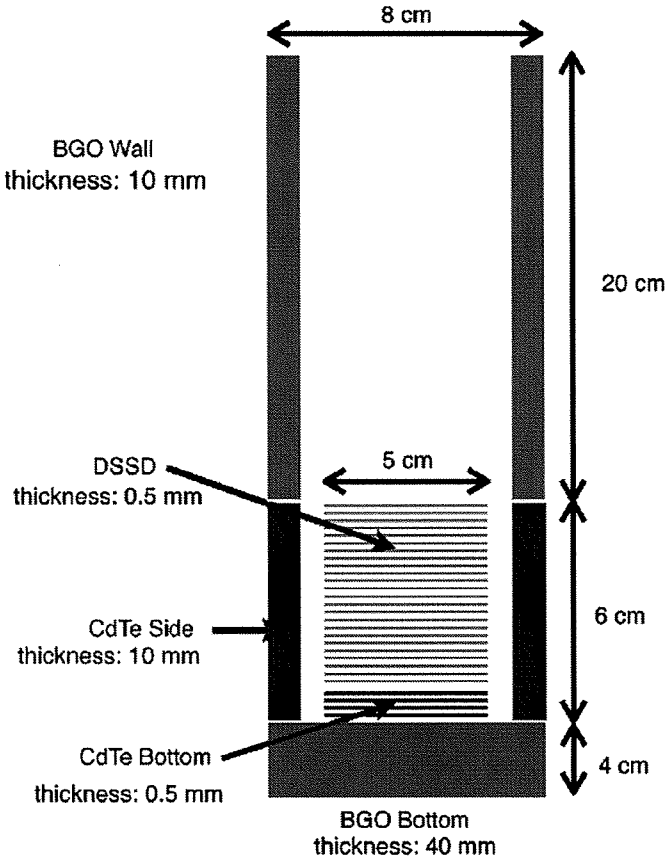

Fig. 2. The simulated geometry of the Si/CdTe Compton telescope.

resolution is assumed to be 1.5 keV (full-width at half-maximum, FWHM), as demonstrated in our previous prototype (also see Ref. [17]). Four layers of CdTe pixel detectors (CdTe Bottom) are also formed as another stack and are placed under the stacked DSSDs. Each CdTe detector consists of 25 × 25 pixels and has a size of 50 mm × 50 mm with a thickness of 0.5 mm. The pixel size is 2 mm × 2 mm. In the simulation, each stack has a frame made of silicon simulating the substrate or electronic devices for data readout, which acts as blocking material around the detector. The thickness is 0.5 mm in the default setting. In addition to these, four CdTe detectors (CdTe Side) cover individual sides of the DSSDs. The thickness of the material associated with the CdTe Side is 10 mm. In the default setting, only the inner 0.5 mm of the CdTe Side is activated as a detector and the rest is used as an anti-coincidence shield. The energy resolution of the CdTe detectors are set at 1.5 keV (FWHM). BGO crystals are placed at both the top and the bottom of the Compton camera. The well-type shield is formed by these crystals along with the outer parts of the 4 CdTe Side detectors. The thickness of the BGO is 10 mm on the side and 40 mm at the bottom.

In the simulation, incident photons have a power-law spectrum with a photon index of −2.1 ranging from 50 to 400 keV, and are generated at the top of the detector, irradiating it uniformly, thus emulating signals from a celestial source. We used the Geant4 simulation toolkit [18] to carry out the simulations and included the G4LECS extension of Kippen [19,20] in order to estimate the effect of Doppler broadening. This broadening is due to the finite momentum of bound electrons in an atom and it results in a deterioration of the angular resolution of Compton telescopes [21].

3. Compton reconstruction

The data taken from the Si/CdTe Compton telescope allow for two analysis modes. The first is the photo absorption mode and the second is the Compton mode. In the photo absorption mode, the energy deposited in all layers is summed if the corresponding deposited energy exceeds a threshold energy of the detector.

In the Compton mode, events satisfying a condition that a photon is scattered once and then absorbed are selected. Once the locations and energies of the two interactions are measured, the Compton equation allows the calculation of the energy and the direction (as a cone in the sky) of the incident γ-ray:

$$E_{\mathrm{in}} = E_1 + E_2 \tag{1}$$

$$\cos\theta = 1 - \frac{m_e c^2}{E_2} + \frac{m_e c^2}{E_1 + E_2} \tag{2}$$

where E_1 is the energy deposited by the Compton scattering and E_2 is that deposited by the photo absorption, m_e is the electron mass and c is the speed of light.

An outline of our Compton reconstruction algorithm is as follows:

(1) Event trigger: The target of analysis is events that have at least one hit which has an energy deposit exceeding the trigger energy of 10 keV. Within the event, all hits that deposited energy exceeding 3 keV are identified and collected.
(2) Clustering: Two hits detected at adjacent pixels or strips are combined into one. The energy deposited is the sum of the two and the newly calculated position is the energy-weighted average of the two hit positions. By this operation, an event such that charge is shared between two adjacent pixels or strips is regarded as one hit.
(3) Anti-coincidence: Events which have at least one hit in the active shield (BGO scintillator and a part of the CdTe Side detector) are rejected. The threshold energy is set at 30 keV.
(4) Two-hit selection: After these screenings, events which have two hits are selected.
(5) "Real Compton" selection: The energy of the recoil electron of Compton scattering E_1 is calculated from the other energy deposited E_2 (assumed to be a photo absorption hit) and the measured scatter angle θ. The value of θ is determined geometrically from the positions of the two hits and the incident direction of the photon, i.e. the FOV of the well-type shield. The significance of the difference between the measured and calculated E_1 is estimated taking account the position resolution, energy resolution, and the effect of the Doppler broadening. Finally, events satisfying the criterion that the calculated E_1 be equal to the measured E_1 within a certain error (4σ) are selected.

It is worth discussing the physics of the identification of the interactions. If a hit takes place at the CdTe Side detectors, we can clearly distinguish between photo absorption and Compton scattering via geometrical considerations. For other hit position combinations, other considerations are needed to identify the order of interactions. In the case of $E_{\mathrm{in}} < m_e c^2/2 = 255$ keV, the energy of the recoil electron by Compton scattering E_1 is always lower than E_2. Thus, the identification is simple. On the other hand, when the incident energy E_{in} exceeds $m_e c^2/2 = 255$ keV, E_1 can be larger than E_2. From the simulation, we found that events such that the photon is scattered at CdTe and then absorbed back at Si ("CdTe Bottom–DSSD" events) are rare. The probability is less than 2% of that of the events of reverse order ("DSSD–CdTe Bottom" events) in the energy band from 255 to 400 keV. Considering this result, we assume that a hit at DSSD is a Compton scattering when one hit is at "DSSD" and the other is at "CdTe Bottom". If two hits take place at the same detector type, "DSSD–DSSD" or "CdTe Bottom–CdTe Bottom" events, we calculate the differences between the measured E_1 and the calculated E_1

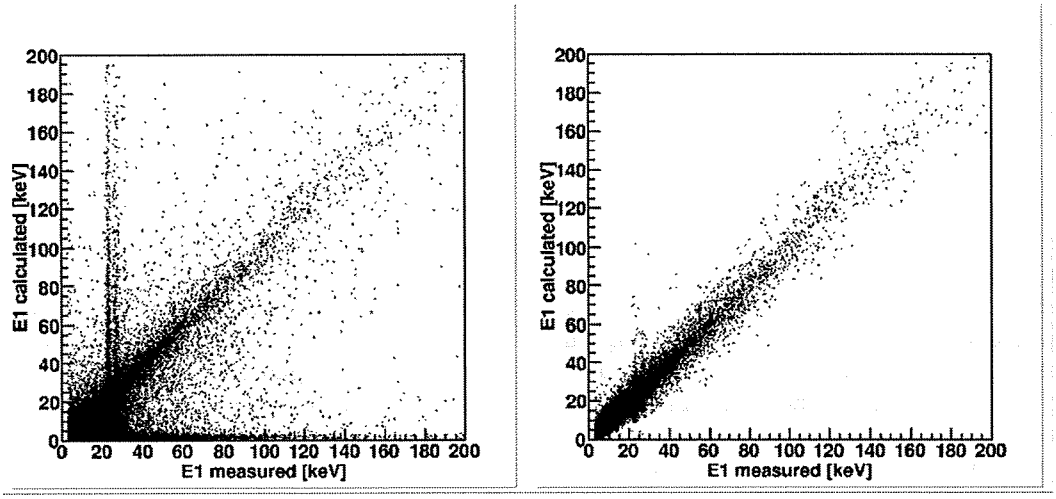

Fig. 3. Comparison of E_1 calculated by Compton reconstruction and actually measured value. The left panel stands for events after the two-hit selection, while the right panel after the "real Compton" selection.

for the two possible orders. We then select the interaction order such that the difference is smaller. By this method, we can determine the "scattering–absorption" order with an accuracy of 99% and 95% for "DSSD–DSSD" and "CdTe Bottom–CdTe Bottom" events, respectively.

Fig. 3 shows the relation between the measured E_1 and the calculated E_1 after the two-hit selection (left) and after the "real Compton" selection (right). In the case of real Compton events, the calculated E_1 is equal to the measured E_1 within the errors. The uncertainty of energy and position measured with the DSSDs and the CdTe pixel detectors contributes to the errors, as does Doppler broadening. After the two-hit selection, there are some bad events such that the calculated E_1 disagrees with the measured E_1. In these events, two hits caused by a fluorescence X-ray emitted from Cd or Te after photo absorption are dominant, being responsible for about 80% of the total of such events. In the left panel of Fig. 3, such events are seen as vertical lines around 20–30 keV. Other sources of error are multiple Compton scatterings or escaped electrons off the detector after photo absorption. Most of the bad events are removed after the "real Compton" selection as shown in the right panel of Fig. 3. For example, more than 90% of the fluorescence X-ray events are rejected by this selection.

4. Detection efficiency

The detection efficiencies in the two different data analysis modes are presented in Fig. 4. For simplicity we hereafter separate the energy band into six bands, 50–70, 70–100, 100–140, 140–200, 200–280, and 280–400 keV. The efficiency of the Compton mode exceeds 10% in the three energy bands below ~120 keV.

Since the Compton camera is composed of DSSDs, CdTe pixel detectors at the bottom (CdTe Bottom), and CdTe pixel detectors at the sides (CdTe Side), we can classify Compton-reconstructed events into six

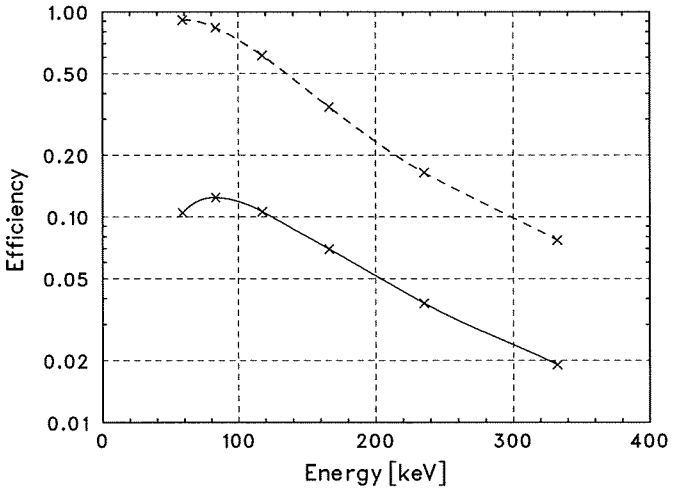

Fig. 4. Detection efficiency of the photo absorption mode (dashed line) and the Compton mode (solid line).

patterns according to their interaction positions, i.e. their detector type. Fig. 5 shows the relative ratio of hit positions of the "scatterring–absorption" events in various energy ranges. The fraction of "DSSD–CdTe Side" events are dominant in all energy bands. Below 100 keV, the probability of "DSSD–DSSD" events is the second highest. As the energy increases, the probability of "DSSD–CdTe Bottom" events or "CdTe Bottom–CdTe Bottom" events increases.

Using the simulations, we evaluated what parameters of the detector design affect the detection efficiency significantly. Fig. 6 shows the detection efficiency as a function of the incident energy for different total thickness of CdTe Bottom detectors. In the default configuration, the total thickness is 2 mm using four layers of CdTe detectors. A thickness of 0.5 mm is sufficient to stop photons below 70 keV. Above 100 keV, setting the total thickness of the CdTe Bottom to 1 mm or greater increases the detection efficiency by a factor of 1.3–1.5.

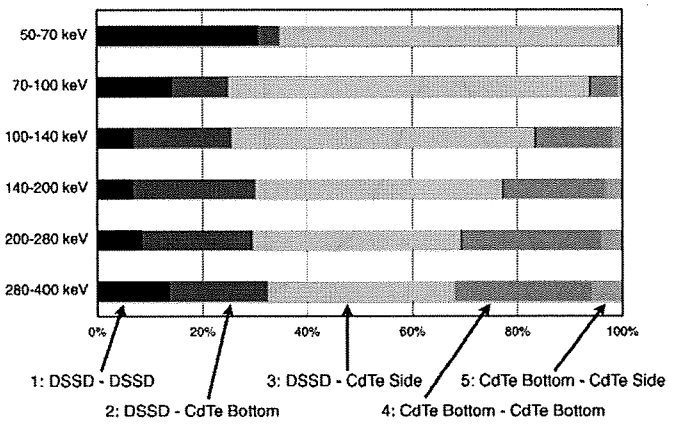

Fig. 5. Relative ratio of hit positions in the six energy bands. 1: "DSSD–DSSD" events, 2: "DSSD–CdTe Bottom" events, 3: "DSSD–CdTe Side" events, 4: "CdTe Bottom–CdTe Bottom" events, and 5: "CdTe Bottom–CdTe Side" events are shown in this order from the left to the right. "CdTe Bottom – DSSD" events are so rare that they cannot be seen in this figure.

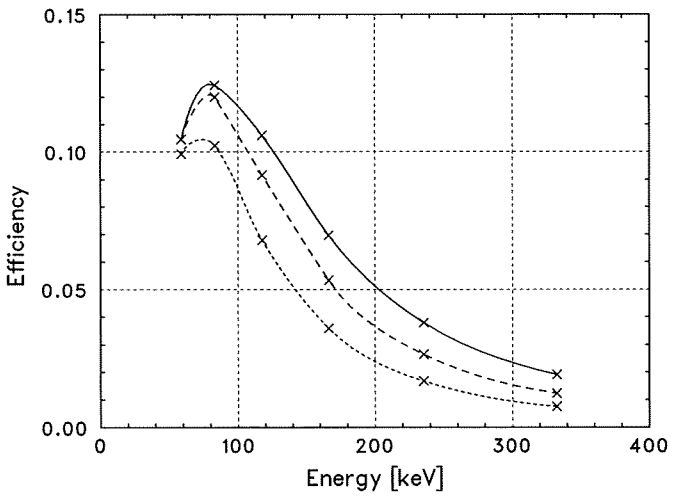

Fig. 6. Detection efficiency in Compton mode with different numbers of activated CdTe Bottom layers; results for four layers (solid), two layers (dashed) and one layer (dotted) are presented. They are equivalent to thickness of 2.0, 1.0, and 0.5 mm, respectively.

Fig. 7 is similar to Fig. 6, but for different total thicknesses of the CdTe Side detectors. The default value is 0.5 mm, which is equivalent to one layer of the CdTe pixel detector employed at the bottom layers. The detection efficiency gets much better as the thickness increases. The efficiency with 1.5 mm thickness exceeds 15% at around 100 keV. Since producing a high resolution CdTe detector thicker than 0.75 mm is technically difficult, increasing the number of layers will be a choice, even though the total number of channels will increase significantly. Adding more CdTe layers at the side improves the detection efficiency better than adding to the bottom for gamma-rays below 300 keV. This result agrees with the large proportion of "DSSD–CdTe Side events" throughout the energy band in this study.

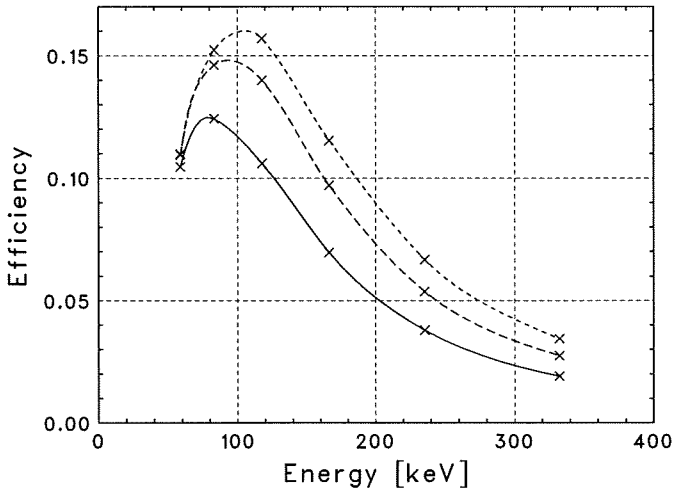

Fig. 7. Detection efficiency in Compton mode with different values of thickness of activated CdTe Side detector; results for 0.5 mm (solid), 1.0 mm (dashed), and 1.5 mm (dotted) are presented.

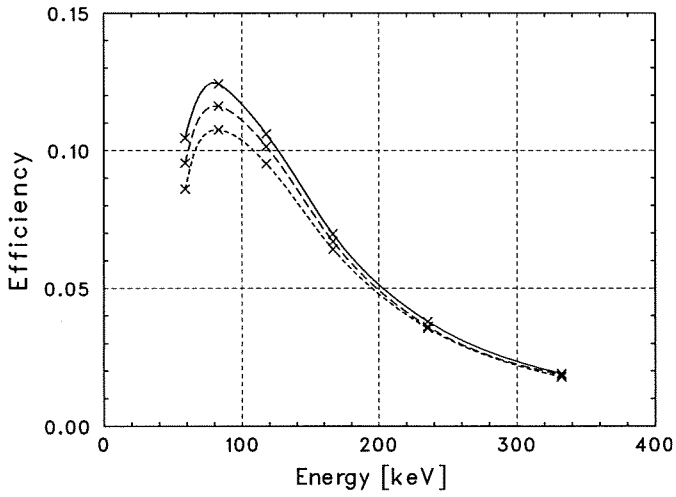

Fig. 8. Detection efficiency in Compton mode for different thickness of Si passive materials around detectors; results with 0.5 mm (solid), 2.0 mm (dashed), and 4.0 mm (dotted) are presented.

Materials surrounding the detectors, such as substrates and electronic devices for data readout, block photons and decrease the efficiency. The efficiency for several cases of the detector frame thickness is shown in Fig. 8. The material is approximated as pure Si. The effect is not important in the high energy range above a few hundred keV, but is significant below 100 keV.

5. Angular resolution

In this section we evaluate the angular resolution of the Si/CdTe Compton telescope. We define the angular resolution measure (ARM) as $\Delta\theta = \theta_{\text{energy}} - \theta_{\text{geom}}$. Here θ_{energy} is the scatter angle calculated from energy deposits E_1, E_2, and θ_{geom} is that determined from hit positions geometrically. The ARM distributions in the six energy bands are shown in Fig. 9. In this figure, we use only the

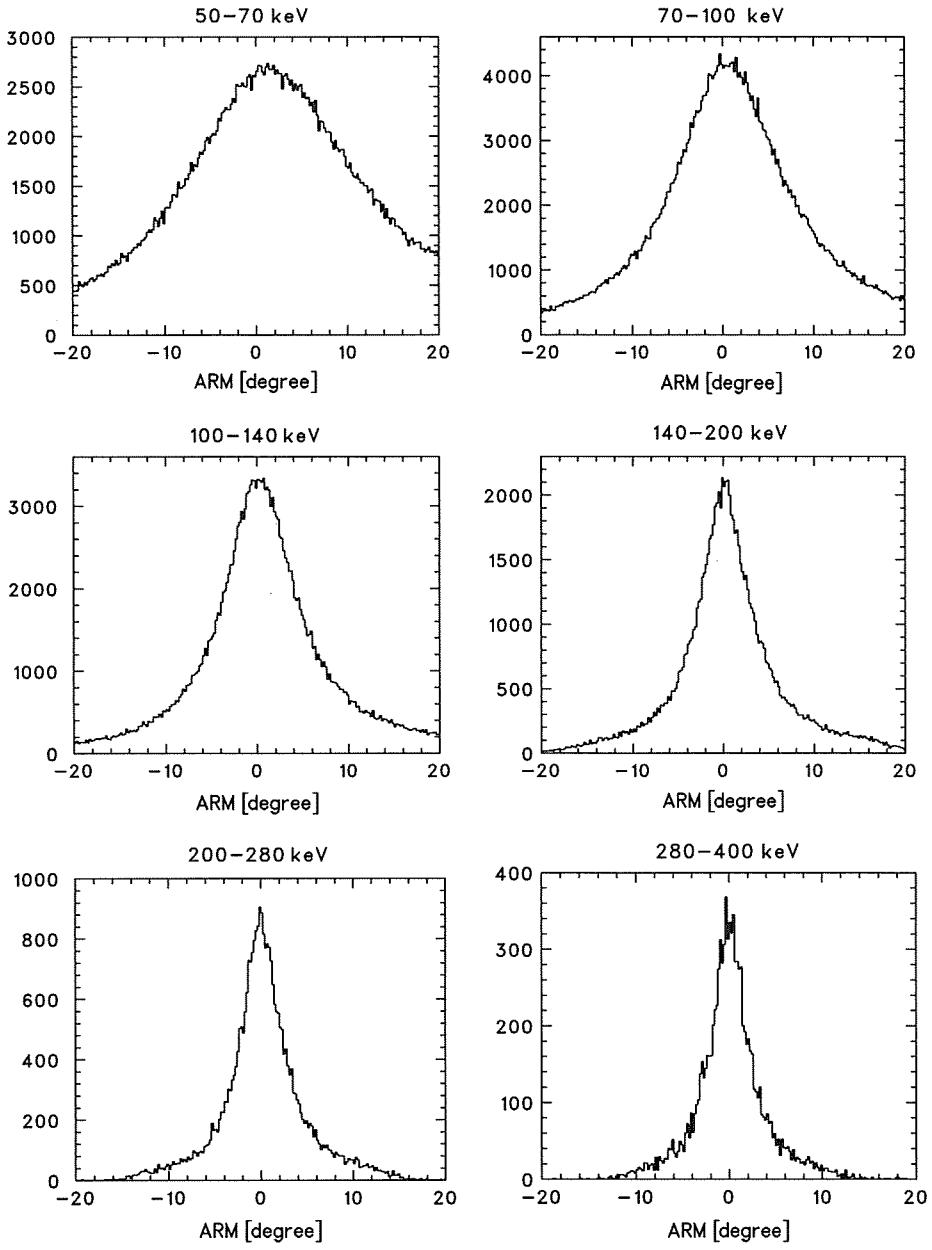

Fig. 9. Distribution of the ARM ($\Delta\theta = \theta_{\text{energy}} - \theta_{\text{geom}}$), in the six energy bands.

"DSSD–CdTe Bottom" and the "DSSD–CdTe Side" events. As noted later in this section, the CdTe scattered events significantly deteriorate the angular resolution due to its large Doppler broadening.

The FWHM of the ARM distribution is one indicator of the angular resolution. The thick solid line in Fig. 10 shows the FWHM of the ARM distribution, $\Delta\theta_{\text{total}}$, as a function of the incident energy. As the energy increases, the angular resolution becomes better. It amounts to 9° at 120 keV, and 4.4° at 330 keV.

The distribution of the ARM originates from three main components: the position resolution, the energy resolution, and the Doppler broadening. Using the case of the energy band from 140 to 200 keV, we present every contribution separately by calculating the ARMs including each effect in Fig. 11. The distributions of scatter caused by the position resolution ($\Delta\theta_{\text{pos}}$) and that by the energy resolution ($\Delta\theta_{\text{ene}}$) are Gaussian-like. In contrast, that of the Doppler broadening effect ($\Delta\theta_{\text{DB}}$) has a narrow peak with broad non-Gaussian wings. Because the effect of these wings is significant when the three components are convoluted, the FWHM of the $\Delta\theta_{\text{DB}}$ distribution underestimates the contribution of the Doppler broadening effect. In order to avoid this problem, we redefined the contribution from the Doppler broadening effect as

$$\Delta\theta_{\text{DB}} = \sqrt{(\Delta\theta_{\text{total}})^2 - (\Delta\theta_{\text{pos}})^2 - (\Delta\theta_{\text{ene}})^2}. \quad (3)$$

Please note that the redefined $\Delta\theta_{\text{DB}}$ is not independent of the position and energy resolutions of the detectors.

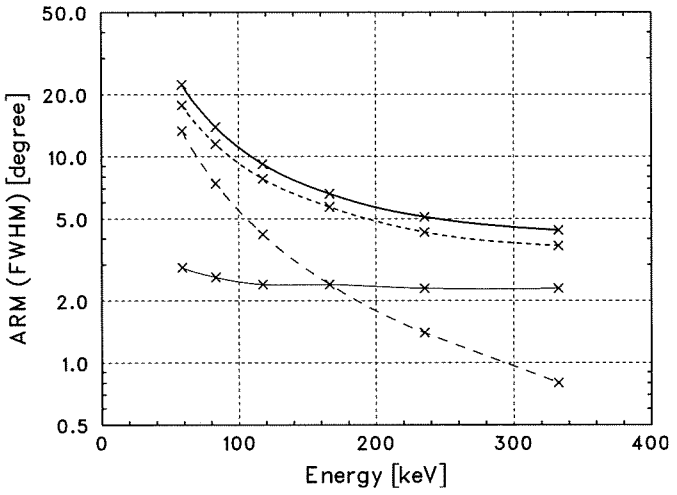

Fig. 10. FWHM of the ARM ($\Delta\theta_{tot}$: thick solid line) as a function of the incident photon energy. Contributions by the energy resolution ($\Delta\theta_{ene}$: dashed), by the position resolution ($\Delta\theta_{pos}$: thin solid line), and by the Doppler broadening effect ($\Delta\theta_{DB}$: dotted line) are also presented. See text for detail.

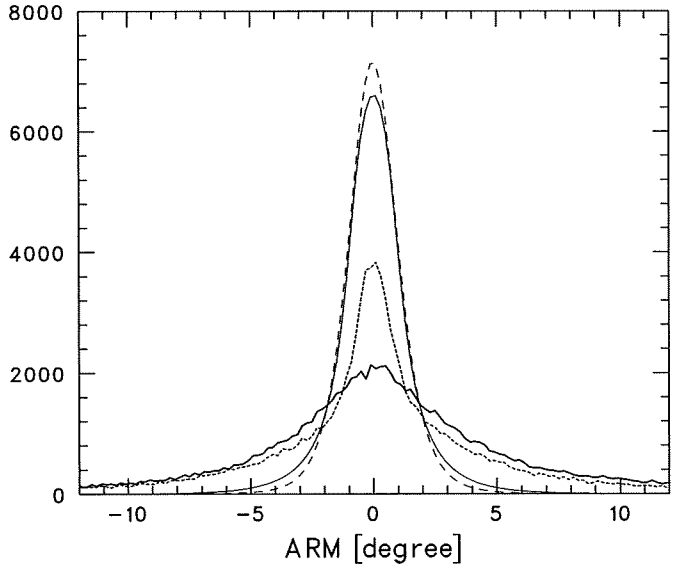

Fig. 11. The ARM distribution profile in the energy band from 140 to 200 keV (thick solid line). Contributions by the energy resolution ($\Delta\theta_{ene}$: dashed line), by the position resolution ($\Delta\theta_{pos}$: thin solid line), and by the Doppler broadening effect ($\Delta\theta_{DB}$: dotted line) are also presented.

The three components thus defined as a function of the incident energy are superposed in Fig. 10. The contribution from the Doppler broadening is a major component in all energy bands. Below 100 keV, the energy resolution limits the angular resolution. In the energy range higher than 200 keV, the angular resolution is limited mainly by the position resolution of the detector. If we are able to prepare CdTe pixel detectors with the finer pixel pitch of 400 μm, the same as that of the DSSDs, the FWHM of the ARM distribution is greatly improved from 4.4° to 2.6° at 330 keV. Note that this significant improvement is achieved

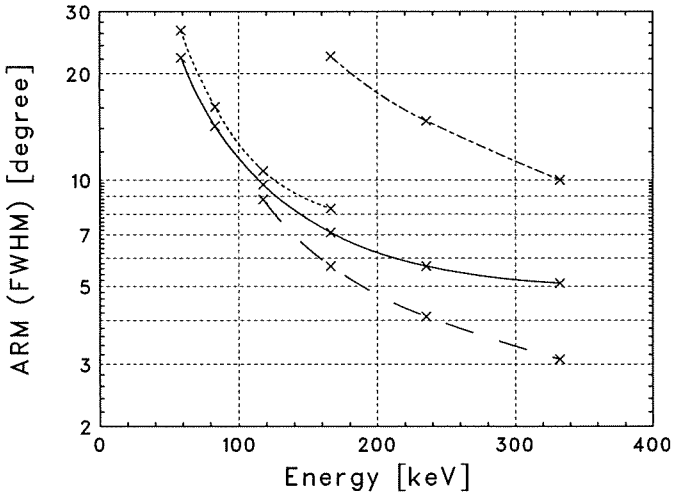

Fig. 12. The ARM of various hit positions: "DSSD–DSSD" events (dotted), "DSSD–CdTe Bottom" events (dashed), "DSSD–CdTe Side" events (solid), and "CdTe Bottom–CdTe Bottom" events (dotdash) are presented.

because the position resolution becomes smaller than the core of the Doppler broadening.

Fig. 12 shows the angular resolution for the various event types classified by hit positions (described in Section 4). We find that "DSSD–CdTe Bottom" events give the best angular resolution. At 330 keV, FWHM of the ARM with these events is 3.1°. In contrast, since the Doppler broadening of CdTe is large, CdTe detectors are not suitable as scatterers for high angular resolution Compton cameras. For example, the ARM of "CdTe Bottom–CdTe Bottom" events is significantly worse when compared to the DSSD-scattered events.

6. Conclusion

We carried out Monte Carlo simulations to evaluate the performances of the proposed narrow-FOV Si/CdTe Compton telescope, the SGD, for the NeXT mission. The detection efficiency in the Compton mode at ~100 keV is more than 10%. It is shown that the CdTe Side detectors play an important role in achieving better detection efficiency at ~100 keV. A few degrees of the angular resolution is obtained due to the small Doppler broadening effect of Si, combined with the high energy and position resolution of both the DSSDs and CdTe pixel detectors. At 330 keV, FWHM of ARM is 4.4 keV and it is improved to 3.1° if "DSSD–CdTe Bottom" events are selected. This result is the same level of the proposed Advanced Compton Telescope, which has an angular resolution of 3.3° at ~300 keV [22]. Since our detector is optimized for a lower energy band compared with other Compton telescopes, Compton reconstruction works with the Si/CdTe Compton telescope at lower energy such as ~80 keV. For example, an angular resolution of 9° is obtained for gamma-rays with an energy of 120 keV, which is very low for a Compton

telescope. For the next step, studies of activation backgrounds caused by cosmic rays in orbit and the evaluation of the capability to reject such backgrounds is indispensable to determine detailed parameters of the detector. A Geant4 based Monte Carlo program with a capability to handle activation in the material is now being set up.

References

[1] V. Schönfelder, et al., ApJ Suppl. 86 (1993) 657.
[2] V. Schönfelder, et al., Astron. Astrophys. Suppl. 120 (1996) 13.
[3] V. Schönfelder, et al., Astron. Astrophys. Suppl. 143 (2000) 145.
[4] V. Schönfelder, New Astron. Rev. 48 (2004) 193.
[5] T. Kamae, R. Enomoto, N. Harada, Nucl. Instr. and Meth. A 260 (1987) 254.
[6] Y.F. Du, Z. He, G.F. Knoll, D.K. Wehe, W. Li, Nucl. Instr. and Meth. A 457 (2001) 203.
[7] J.D. Kurfess, W.N. Johnson, R.A. Kroeger, B.F. Phlips, E.A. Wulf, Nucl. Instr. and Meth. A 505 (2003) 256.
[8] T.J. O'Neill, D. Bhattacharya, M. Polsen, A.D. Zych, J. Samimi, A. Akyuz, IEEE Trans. Nucl. Sci. NS-50 (2003) 251.
[9] T. Takahashi, K. Nakazawa, T. Kamae, H. Tajima, Y. Fukazawa, M. Nomachi, M. Kokubun, Proc. SPIE 4851 (2003) 1228.
[10] G. Kanbach, et al., New Astron. Rev. 48 (2004) 275.
[11] T. Tanaka, et al., Proc. SPIE 5501 (2004) 229.
[12] S. Watanabe, et al., IEEE Trans. Nucl. Sci. NS-52 (2005) 2045.
[13] T. Tanaka, et al., Nucl. Instr. and Meth. A 568 (2006) 375.
[14] T. Takahashi, K. Mitsuda, H. Kunieda, Proc. SPIE 6266 (2006) 62660D.
[15] H. Tajima, et al., IEEE Trans. Nucl. Sci. NS-52 (2005) 2749.
[16] T. Takahashi, et al., Proc. SPIE 5488 (2004) 549.
[17] S. Takeda, et al., Nucl. Instr. and Meth. A (2007).
[18] Geant4, ⟨http://geant4.web.cern.ch/geant4/⟩.
[19] G4LECS, ⟨http://public.lanl.gov/mkippen/actsim/g4lecs/⟩.
[20] R.M. Kippen, New Astron. Rev. 48 (2004) 221.
[21] A. Zoglauer, G. Kanbach, Proc. SPIE 4851 (2003) 1302.
[22] S.E. Boggs, et al., The Advanced Compton Telescope Mission, astro-ph/0608532, (2006).

Japanese Journal of Applied Physics
Vol. 46, No. 9A, 2007, pp. 6043–6045

New CdTe Pixel Gamma-Ray Detector with Pixelated Al Schottky Anodes

Shin WATANABE[1,2*], Shin-nosuke ISHIKAWA[1,2], Shin'ichiro TAKEDA[1,2], Hirokazu ODAKA[1,2], Takaaki TANAKA[3], Tadayuki TAKAHASHI[1,2], Kazuhiro NAKAZAWA[2], Masaaki YAMAZATO[4], Akira HIGA[4], and Sakari KANEKU[5]

[1]*Institute of Space and Astronautical Science, Japan Aerospace Exploration Agency, 3-1-1 Yoshinodai, Sagamihara, Kanagawa 229-8510, Japan*
[2]*Department of Physics, The University of Tokyo, Bunkyo, Tokyo 113-0033, Japan*
[3]*Stanford Linear Accelerator Center, Menlo Park, CA 94025, U.S.A.*
[4]*Faculty of Engineering, University of the Ryukyus, 1 Senbaru, Nishihara, Okinawa 930-0213, Japan*
[5]*ACRORAD Co., Ltd., Uruma, Okinawa 904-2234, Japan*

(Received May 9, 2007; accepted May 25, 2007; published online September 7, 2007)

We developed a new Al Schottky CdTe pixel detector and measured its spectral performance. It has pixelated anodes made of aluminum and a common cathode made of platinum. Because of the low leakage current and the high bias voltage owing to the Schottky diode characteristic and the anode pixel configuration, a good spectral performance including a high energy resolution was achieved. When the pixel detector with a thickness of 0.75 mm was subjected to a bias voltage of 400 V and was operated at −20 °C, the full-width-half-maximum (FWHM) energy resolution of 1.1 and 1.8 keV at 59.5 and 122 keV, respectively, were successfully obtained. The spectral performance obtained with the Al Schottky CdTe pixel detector exceeded that obtained with the conventional In Schottky CdTe pixel detector, which has an In common anode and Pt pixelated cathodes, under the same operating conditions. [DOI: 10.1143/JJAP.46.6043]

KEYWORDS: gamma-ray detector, cadmium telluride (CdTe), pixel detector

1. Introduction

Hard X-ray and gamma-ray imaging spectrometers with good spatial and energy resolutions are desired for medical, industrial and astrophysical applications. Cadmium telluride (CdTe) and cadmium zinc telluride (CZT) are very promising materials as hard X-ray and gamma-ray imaging spectrometers, because they have a high detection efficiency comparable to that of NaI scintilators and have a good energy resolution comparable to that of Ge detectors. Although a weak point of CdTe and CZT was the degradation of energy resolution and peak detection efficiency owing to poor charge transport properties of their materials, several techniques have been developed to maintain good spectral performance.[1,2)]

In recent years, we have successfully overcome the poor charge transport properties by adopting a thin CdTe diode device. The basic idea of using a CdTe diode is to utilize indium (In) as the anode electrode on a p-type CdTe wafer and platinum (Pt) as the cathode.[1,3,4)] A high Schottky barrier formed on the In/p-CdTe interface leads us to the use of the detector as a diode. Using this type of detector with a thickness of 0.5 mm at an applied bias voltage as high as 1 kV, we have obtained high energy resolutions: 830 eV (full-width-half-maximum: FWHM) at 59.5 keV and 2.1 keV (FWHM) at 662 keV.[1,4)]

On the basis of the In Schottky diode device, we have developed CdTe diode pixel detectors, utilizing In as the common anode and Pt as the pixelated cathode (In/CdTe/Pt-pixel).[4–6)] Because of their Schottky diode characteristic, low leakage current and good energy resolution have been achieved from the In/CdTe/Pt-pixel configuration. Ideally, electrons, which have a larger mobility and a longer lifetime than holes in CdTe, have to be collected for high energy resolution, therefore, the anode side should be pixelated. However, with the current electrode technology, it is difficult to divide an In electrode into pixels.

Recently, as an electrode material, aluminum (Al) has been found to be a good alternative to In.[7,8)] In addition to low leakage current and high energy resolution comparable to those of In/CdTe/Pt detectors, Al/CdTe/Pt detectors have an advantage that an Al anode can be divided into pixels. Therefore, it is possible to fabricate electron-collecting-type diode pixel detectors, utilizing Al as pixelated anodes and Pt as the common cathode (Al-pixel/CdTe/Pt).

We have constructed the first Al-pixel/CdTe/Pt detector using the same components as those used in our recent In/CdTe/Pt-pixel detectors. In this paper, we report the achieved performance of the Al-pixel/CdTe/Pt detector. A comparison between the Al-pixel/CdTe/Pt and In/CdTe/Pt-pixel detectors is also described.

2. Setup of the Al Schottky CdTe Pixel Detector

Figure 1 shows a picture of the Al-pixel/CdTe/Pt detector together with the In/CdTe/Pt-pixel detector. The CdTe device has a size of $13.35 \times 13.35\,mm^2$ and a thickness of 0.75 mm. The CdTe crystal is manufactured

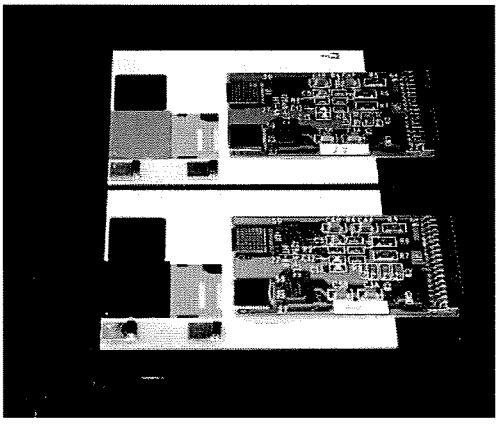

Fig. 1. Picture of the CdTe pixel detectors. The bottom shows the Al-pixel/CdTe/Pt detector and the top shows the In/CdTe/Pt-pixel detector.

*E-mail address: watanabe@astro.isas.jaxa.jp

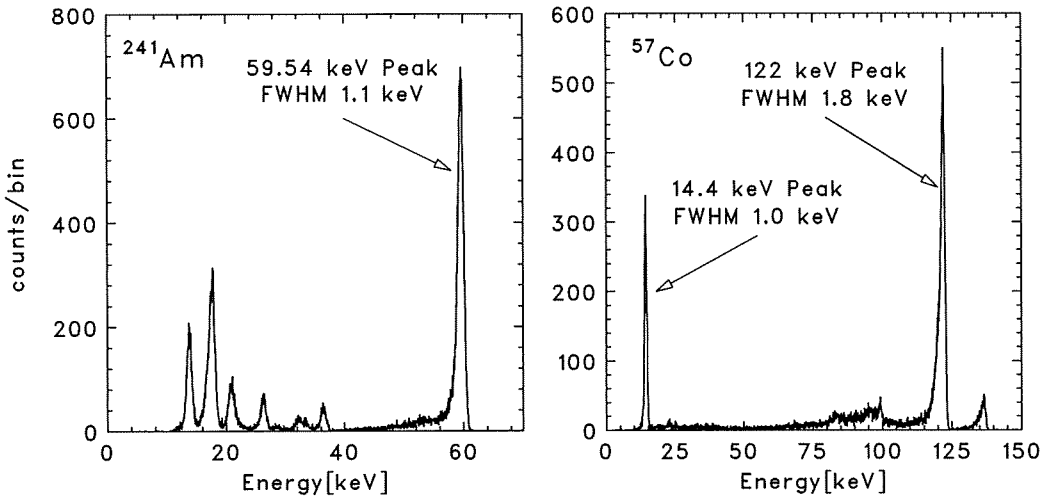

Fig. 2. ^{241}Am and ^{57}Co spectra obtained with one pixel of the Al/CdTe/Pt-pixel detector. The operating temperature was −20 °C, and, the applied bias voltage was −400 V for the Pt common electrode. The achieved FWHM energy resolutions were 1.0, 1.1, and 1.8 keV at 14.4, 59.5, and 122 keV, respectively.

by ACRORAD in Japan using the traveling heater method (THM). The Pt side is used as the common electrode and the Al side is divided into $8 \times 8 = 64$ pixels. The pixel size is $1.35 \times 1.35\,mm^2$, and the gap between the pixel electrode is 50 μm. Around the pixels, a guard ring electrode with a width of 1 mm is attached. Additionally, a thin layer of gold is evaporated on the Al pixel side to ensure a good bump bonding connectivity.

The procedure for the component mounting is the same as that for In/CdTe/Pt-pixel detectors.[6] ASIC for both pixel detectors readout is VA64TA, which was developed by this research team in conjunction with IDEAS and SLAC.[9]

3. Spectral Performance of the Al Schottky CdTe Pixel Detector

In order to evaluate the spectral performance of the Al-pixel/CdTe/Pt detector, we operated the detector in a thermostatic chamber at −20 °C. The applied bias voltage was −400 V for the Pt common cathode. Spectroscopy measurements were performed using gamma-rays from ^{241}Am and ^{57}Co sources.

The spectra obtained from one of the pixels with the best performance are shown in Fig. 2. High energy resolutions were obtained: 1.0 keV (FWHM) at 14.4 keV, 1.1 keV (FWHM) at 59.5 keV, and 1.8 keV (FWHM) at 122 keV. Figure 3 shows the distribution of energy resolution from all 64 pixels. The FWHM spread is within about 10% for almost all pixels. The energy resolutions in the summed spectrum of all 64 pixels were 1.3 keV (FWHM) and 2.0 keV (FWHM) at 59.5 keV and 122 keV, respectively. Additionally, it was found that the long-term stability in the spectrum is sufficient for practical use under our operating conditions. Any significant deteriorations in energy resolution and detection efficiency have not been observed for at least one hour after applying bias voltage.

4. Comparison between the Two Types of CdTe Diode Pixel Detectors

In order to study the effect of the spectral response on the difference in electrode configuration between the Al-pixel/CdTe/Pt and In/CdTe/Pt-pixel detectors, both types of

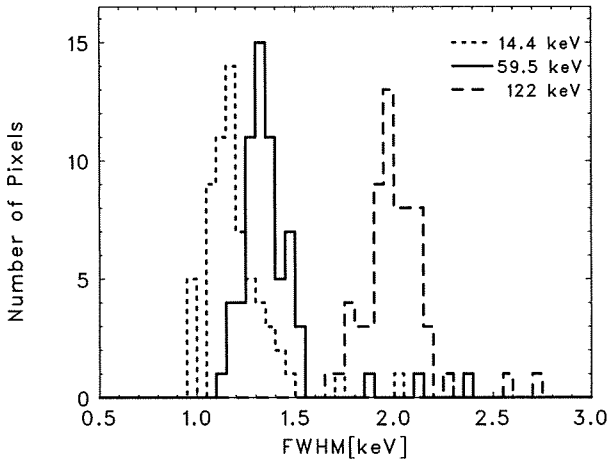

Fig. 3. Distribution of energy resolution from all 64 pixels of the Al-pixel/CdTe/Pt detector.

CdTe device with the same dimension ($13.35 \times 13.35 \times 0.75\,mm^3$) were prepared (Fig. 1). The detectors were operated at −20 °C. We examined the changes of the spectral shape in the 122 keV peak from a ^{57}Co source at various bias voltages.

Figure 4 shows the peak shapes for 122 keV gamma-ray photons obtained using the two types of pixel detector. The sums of the spectra from all pixels are shown. The applied bias voltages are from −100 to −400 V for the Al-pixel/CdTe/Pt detector, and from 100 to 1000 V for the In/CdTe/Pt-pixel detector. The energy scales of the two detector are calibrated on the basis of the spectra of −400 and 1000 V bias, respectively.

In order to quantify the peak heights and the lower tail amounts, the ratios of 120–124 keV count rate to 110–124 keV count rate are plotted as a function of applied bias voltage in Fig. 5. The filled circles and the open circles show the data of Al-pixel/CdTe/Pt and In/CdTe/Pt-pixel detectors, respectively. A higher ratio means a sharper peak and a smaller tail.

Compared with the case of using the In/CdTe/Pt-pixel detector, a small tail and a high peak can be obtained with

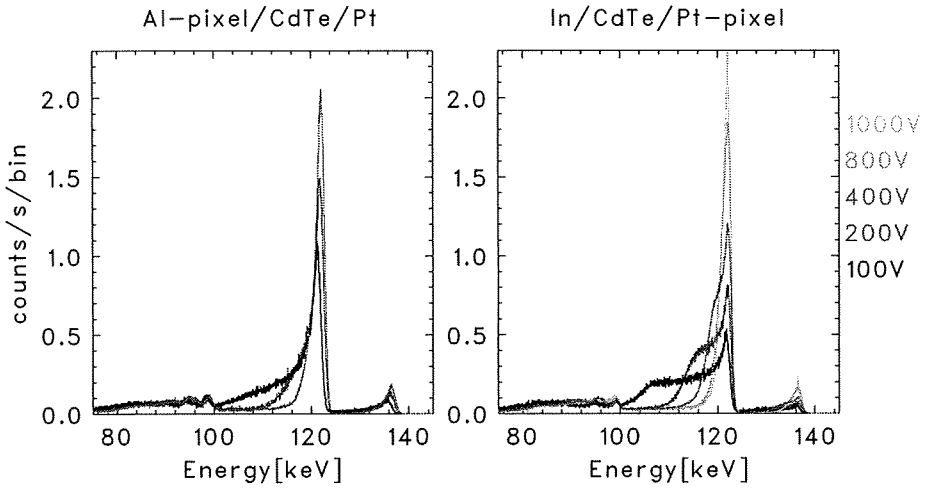

Fig. 4. Spectral changes of the 122 keV peak that are caused by the bias voltage. Left: Spectra obtained with the Al-pixel/CdTe/Pt detector. Bias voltages of −100, −200, and −400 V were applied to the Pt common cathode. Right: Spectra obtained with the In/CdTe/Pt-pixel detector. Bias voltages of 100, 200, 400, 800, and 1000 V were applied to the In common anode. Both detectors were operated at −20 °C. The thickness of the detectors was 0.75 mm. The spectra from all pixels were summed. The energy scales of Al-pixel/CdTe/Pt and In/CdTe/Pt-pixel were calibrated on the basis of the spectra of −400 and 1000 V bias, respectively.

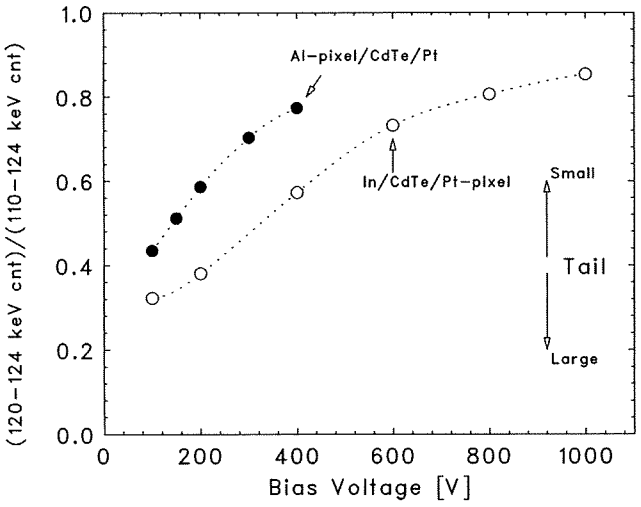

Fig. 5. Characteristics of 122 keV peak shapes. The ratios of 120–124 keV count rate to 110–124 keV count rate are plotted as a function of bias voltage. Filled circles show the data obtained using the Al-pixel/CdTe/Pt detector, and open circles show the data obtained using the In/CdTe/Pt-pixel detector.

the Al-pixel/CdTe/Pt detector under the same bias voltage condition. The peak obtained with the Al-pixel/CdTe/Pt detector under the bias voltage of −400 V is almost equivalent to the peak obtained with the In/CdTe/Pt-pixel detector under the bias voltage of 800 V. The spectral difference should be caused by the $\mu\tau$ product difference between electrons and holes in the CdTe crystal (μ, mobility; τ, lifetime). In the THM CdTe crystals manufactured by ACRORAD, the $\mu\tau$ product of electrons is 10–30 times larger than that of holes.[10] In the case of using the Al-pixel/CdTe/Pt detector, because electrons incoming to the pixel electrodes produce a large part of the signal, there is an advantage in spectral performance. On the other hand, in the case of using the In/CdTe/Pt-pixel detector, small $\mu\tau$ holes should be moved to the cathode pixels. Therefore, a higher bias voltage was required for obtaining a good spectral performance.

5. Conclusions

We have constructed a new type of CdTe pixel diode detector with a Pt common cathode and Al pixelated anodes. The construction procedure was the same as that for our conventional CdTe pixel diode detector with an In common anode and Pt pixelated cathodes. When we applied a bias voltage of 400 V to a 0.75-mm-thick detector and operated at −20 °C, the pixel detector worked successfully and a good energy resolution was achieved. The obtained energy resolutions of one pixel were 1.1 keV (FWHM) at 59.5 keV and 1.8 keV (FWHM) at 122 keV under these conditions. Additionally, we compared the spectral performance between the Al-pixel/CdTe/Pt and In/CdTe/Pt-pixel detectors. It was found that a better energy resolution can be obtained with the Al-pixel/CdTe/Pt detector than with the In/CdTe/Pt-pixel detector under the same bias voltage condition.

1) T. Takahashi and S. Watanabe: IEEE Trans. Nucl. Sci. **48** (2001) 950.
2) O. Limousin: Nucl. Instrum. Methods Phys. Res., Sect. A **504** (2003) 24.
3) T. Takahashi, B. Paul, K. Hirose, C. Matsumoto, R. Ohno, T. Ozaki, K. Mori, and Y. Tomita: Nucl. Instrum. Methods Phys. Res., Sect. A **436** (1999) 111.
4) T. Takahashi, S. Watanabe, G. Sato, Y. Okada, S. Kubo, Y. Kuroda, M. Onishi, and R. Ohno: IEEE Trans. Nucl. Sci. **48** (2001) 287.
5) T. Mitani, T. Tanaka, K. Nakazawa, T. Takahashi, T. Takashima, H. Tajima, H. Nakamura, M. Nomachi, T. Nakamoto, and Y. Fukazawa: IEEE Trans. Nucl. Sci. **51** (2004) 2432.
6) S. Watanabe, S. Takeda, S. Ishikawa, H. Odaka, M. Ushio, T. Tanaka, K. Nakazawa, T. Takahashi, H. Tajima, Y. Fukazawa, Y. Kuroda, and M. Onishi: to be published in Nucl. Instrum. Methods Phys. Res., Sect. A.
7) H. Toyama, A. Nishihira, M. Yamazato, A. Higa, T. Maehama, R. Ohno, and M. Toguchi: Jpn. J. Appl. Phys. **43** (2004) 6371.
8) H. Toyama, M. Yamazato, A. Higa, T. Maehama, R. Ohno, and M. Toguchi: Jpn. J. Appl. Phys. **44** (2005) 6742.
9) T. Tanaka, S. Watanabe, S. Takeda, K. Oonuki, T. Mitani, K. Nakazawa, T. Takashima, T. Takahashi, H. Tajima, N. Sawamoto, Y. Fukazawa, and M. Nomachi: Nucl. Instrum. Methods Phys. Res., Sect. A **568** (2006) 375.
10) G. Sato, T. Takahashi, M. Sugiho, M. Kouda, T. Mitani, K. Nakazawa, Y. Okada, and S. Watanabe: IEEE Trans. Nucl. Sci. **49** (2002) 1258.

Journal of Nuclear and Radiochemical Sciences, Vol. 8, No. 2, pp. 55-58, 2007

Development of Gas-jet Transport System Coupled to the RIKEN Gas-filled Recoil Ion Separator GARIS for Superheavy Element Chemistry

H. Haba,*[a] D. Kaji,[a] H. Kikunaga,[a] T. Akiyama,[a,b] N. Sato,[a,c] K. Morimoto,[a] A. Yoneda,[a] K. Morita,[a] T. Takabe,[d] and A. Shinohara[d]

[a]*Nishina Center for Accelerator Based Science, RIKEN, Wako, Saitama 351-0198, Japan*
[b]*Department of Physics, Saitama University, Sakura, Saitama 338-8570, Japan*
[c]*Department of Physics, Tohoku University, Aoba, Sendai 980-8578, Japan*
[d]*Graduate School of Science, Osaka University, Toyonaka, Osaka 560-0043, Japan*

Received: January 27, 2007; In Final Form: April 3, 2007

A gas-jet transport system for the superheavy element chemistry was coupled to the gas-filled recoil ion separator GARIS at the RIKEN Linear Accelerator. The performance of the system was investigated using ^{206}Fr and ^{245}Fm produced in the ^{40}Ar-induced reactions on ^{169}Tm and ^{208}Pb targets, respectively. Alpha particles of ^{206}Fr and ^{245}Fm separated with GARIS and transported by the gas-jet were measured with a rotating wheel system for α spectrometry under low background condition. The high gas-jet efficiency of over 80% was found to be independent of the beam intensity up to 2 particle μA. These results suggest that the GARIS/gas-jet system is a promising tool for future superheavy element chemistry at RIKEN.

1. Introduction

The chemistry of the superheavy elements (SHEs) with atomic numbers $Z \geq 104$ has become one of the most exciting and challenging research subjects in nuclear and radiochemistry.[1,2] Experimental studies on chemical properties of SHEs have been performed for elements 104 to 108 and very recently element 112.[1,2] The production rates of the SHE nuclides, however, are extremely low, i.e., atoms per minute for elements 104 (Rf) and 105 (Db) down to atoms per hour or day for elements 106 (Sg) to 108 (Hs),[2] and their half-lives are less than ~1 min. This situation forces us to perform rapid and efficient on-line chemical experiments with "single atoms" using heavy-ion accelerators. The gas-jet transport technique has been commonly used to transfer SHE atoms from a target chamber to various chemistry apparatuses. Here, nuclear reaction products recoiling out of a target are stopped in the chamber filled with helium gas, and are often attached to aerosol particles such as potassium chloride (KCl) and carbon. The gas and activity-laden aerosol particles are swept out through a capillary to a distant site where chemistry apparatuses and detectors are equipped.

SHE atoms are produced among large amounts of background radioactivities which hinder the detection of decay signals of SHE nuclides. Recently available high-intensity beams of more than 1 particle μA (pμA) also give rise to a serious problem in that the plasma formed by the beam in the target chamber significantly reduces the gas-jet transport efficiency. To overcome these situations, it has been proposed that a recoil separator for nuclear physics research on SHEs should be coupled to the chemistry system with the aid of the gas-jet transport technique mentioned above.[1,3] With this method, background radioactivities originating from other reaction products are largely removed. The high and stable gas-jet efficiencies are obtained owing to the condition free from plasma. Furthermore, chemical reactions of various compounds can be studied by directly feeding complexing reagents into the gas-jet chamber without aerosol materials. The first experiment with the recoil transfer chamber (RTC) coupled to the Berkeley Gas-filled Separator (BGS) was very successful.[4,5] The isotope of ^{257}Rf physically separated from the large amount of β-decaying products was identified with a liquid scintillator after a liquid-liquid solvent extraction. Thereafter, the BGS/RTC system was used in the model experiments of Rf (References 6–8) and Hs (Reference 9). At Gesellschaft für Schwerionenforschung (GSI), the components of the former HElium Charge-exchange Kaleidoscope (HECK) separator are being used to set up a dedicated separator for the SHE chemistry.[3]

In the RIKEN Linear Accelerator (RILAC) facility, the gas-filled recoil ion separator GARIS has been used to search for the heaviest SHE nuclides.[10–13] The isotopes of ^{271}Ds, ^{272}Rg, and ^{277}112 found at GSI were confirmed with better statistics and with new spectroscopic information,[10–12] and a new isotope of element 113, ^{278}113, was successfully synthesized.[13] GARIS is expected to give us low background condition and high transport efficiencies for SHEs. In this work, we have installed a gas-jet transport system at the focal plane of GARIS to start the SHE chemistry in RIKEN. The performance of the system was appraised using ^{206}Fr and ^{245}Fm produced in the ^{169}Tm(^{40}Ar,3n)^{206}Fr and ^{208}Pb(^{40}Ar,3n)^{245}Fm reactions, respectively.

2. Experimental

A schematic of the experimental setup is shown in Figure 1. The $^{40}Ar^{9+}$ ion beam was extracted from RILAC. The metallic ^{169}Tm and ^{208}Pb targets of 120 and 420 μg cm^{-2} thicknesses, respectively, were prepared by vacuum evaporation on 30 μg cm^{-2} carbon backing foils. Sixteen targets were mounted on a rotating wheel of 30 cm in diameter. The wheel was rotated during the irradiation at 3000 rpm. The beam energies were 169.7 MeV for ^{169}Tm and 198.6 MeV for ^{208}Pb at the middle of the targets. At these incident energies, the cross section for the ^{169}Tm(^{40}Ar,xn)$^{209-x}$Fr reactions ($x = 2 + 3$) is 376 ± 7 μb,[14] while that for ^{208}Pb(^{40}Ar,3n)^{245}Fm is 15 ± 5 nb.[15] The beam intensity was monitored by measuring elastically scattered projectiles with a Si PIN photodiode (Hamamatsu S1223) mounted at 45° with respect to the beam axis. The typical beam intensity was 2 pμA. GARIS was filled with helium at a pressure of 88 Pa.

*Corresponding author. E-mail: haba@riken.jp. Fax: +81-48-461-5301.

Published on Web 10/19/2007

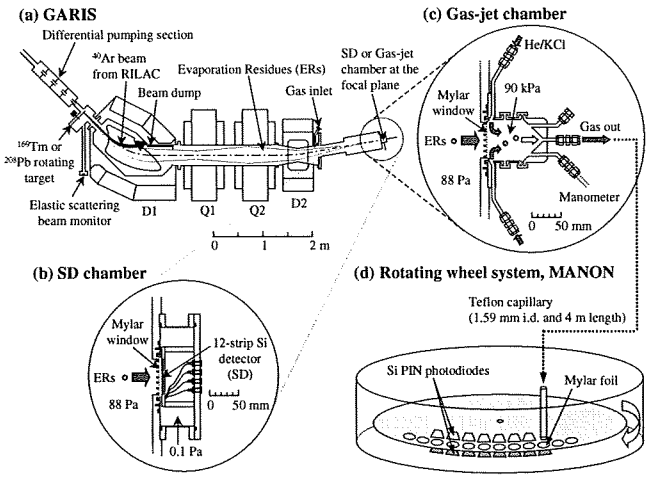

Figure 1. A schematic of the experimental setup: (a) RIKEN gas-filled recoil ion separator GARIS; (b) 12-strip Si detector (SD) chamber; (c) Gas-jet chamber coupled to GARIS; (d) Rotating wheel system MANON for α spectrometry.

The magnetic rigidities were set at 1.64 Tm for ^{206}Fr and at 2.01 Tm for ^{245}Fm. The other details of GARIS are given elsewhere.[11]

As shown in Figures 1(a) and 1(b), the evaporation residues of interest were separated in-flight from beam particles and transfer reaction products with GARIS, and were implanted into a 12-strip Si detector (SD) of 60 × 60 mm^2 (Hamamatsu 12CH PSD) through a Mylar window of 3.5 ± 0.1 μm thickness which was supported with a stainless-steel honeycomb grid with 92.5% transparency and of 60 mm diameter. Alpha-particle measurements of ^{206}Fr were conducted for 2600 s under the beam-on condition and for 300 s after a 30-s beam irradiation. In the ^{245}Fm experiment, the cycle of the beam-on (5 s) and beam-off (15 s) measurements was repeated 1265 times, because no α peak of ^{245}Fm was observed in the beam-on spectrum due to large amounts of background events. The α-particle energy resolution of SD was 50 keV FWHM. All events were registered in an event-by-event mode.

In the gas-jet transport experiments, ^{206}Fr and ^{245}Fm separated by GARIS were guided into the gas-jet chamber of 60 mm length as shown in Figure 1(c). The reaction products were stopped in the helium gas at 90 kPa, attached to KCl aerosol particles generated by sublimation of the KCl powder at 620 °C, and were continuously transported through a Teflon capillary (1.59 mm i.d., 4 m length) to the rotating wheel system MANON for α spectrometry (Figure 1(d)) which was the compact one of the Measurement system for the Alpha-particle and spontaneous fissioN events ON-line developed at Japan Atomic Energy Agency (JAEA).[16] The flow rate of the helium gas was 5 L min^{-1}. In the ^{206}Fr experiment, the temperature of the KCl aerosol generator was varied from 540 to 640 °C in steps of about 20 °C to optimize the gas-jet transport efficiency. In MANON, aerosol particles were deposited on Mylar foils of 0.68 μm thickness and 20 mm diameter placed at the periphery of a 40-position stainless steel wheel of 420 mm diameter. The wheel was stepped at 30-s and 2-s intervals for ^{206}Fr and ^{245}Fm, respectively, to position the foils between seven pairs of Si PIN photodiodes (Hamamatsu S3204-09). Each detector had an active area of 18 × 18 mm^2 and a 38% counting efficiency for α particles. The α-particle energy resolution was 60 keV FWHM for the detectors which look at the sample from the collection side (top detectors).

3. Results and Discussion

Figure 2(a) shows an α-particle spectrum measured in the ^{206}Fr experiment for 2600 s in the 6th strip (middle) of SD under the beam-on condition. Alpha peaks of ^{206}Fr ($T_{1/2}$ = 15.9 s, E_α = 6.790 MeV)[17] and ^{205}Fr (3.85 s, 6.915 MeV)[17] and of their daughter nuclides ^{202}At (182 s, 6.135 MeV; 184 s, 6.228 MeV)[17] and ^{201}At (89 s, 6.344 MeV)[17] were identified. The broad component above 7 MeV is associated with the implantation of evaporation residues (ERs) and target recoils (TRs). Figure 2(b) shows an α-particle spectrum measured in the 6th strip of SD for 300 s after the 30-s beam irradiation. The decay curve of the 6.790-MeV α peak of ^{206}Fr is shown in the inset of Figure 2(b). The half-life of ^{206}Fr was determined to be 15.3 ± 0.2 s, which is in agreement with the literature value of 15.9 ± 0.2 s (Reference 17) within 2σ. The contribution of the α particles of ^{207}Fr (14.8 s, 6.768 MeV)[17] produced in the ^{169}Tm(^{40}Ar,2n)^{207}Fr reaction to the 6.790-MeV peak of ^{206}Fr is found to be negligible from the absence of the 6.087-MeV peak of its daughter nuclide ^{203}At (7.4 min, 6.087 MeV)[17] in Figure 2(a). On the other hand, the α-particle spectrum measured in the first top detector of MANON for 30 s after the 30-s aerosol collection is compared in Figure 2(c). The α peak of ^{206}Fr is clearly seen in

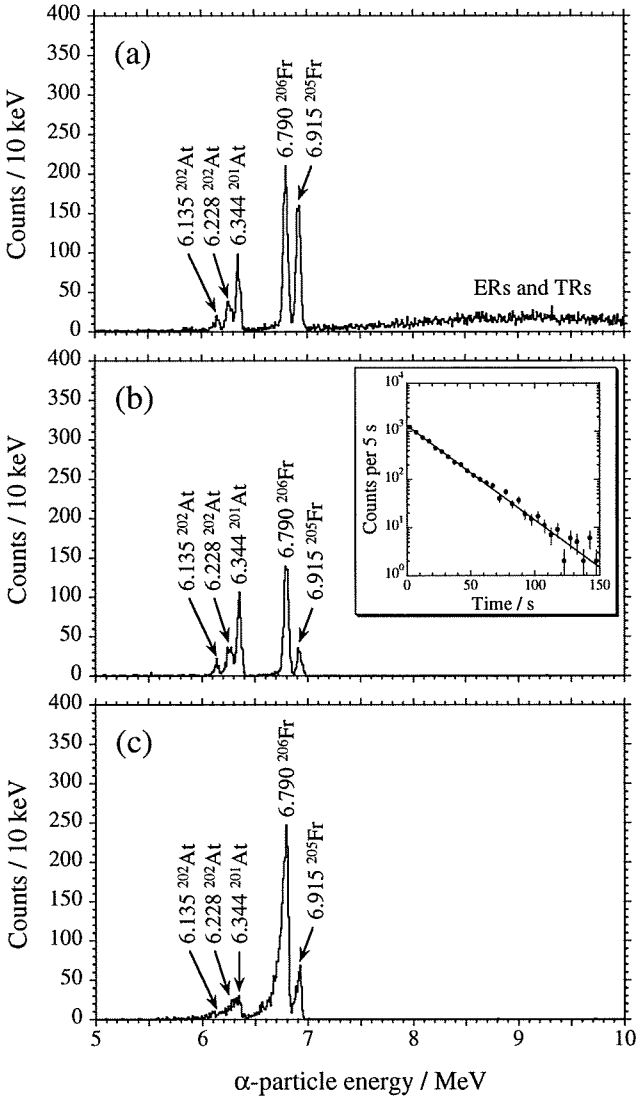

Figure 2. (a) Alpha-particle spectrum measured in the ^{206}Fr experiment for 2600 s in the 6th strip (middle) of the 12-strip Si detector (SD) under the beam-on condition. The ^{40}Ar beam intensity was 0.017 pμA. (b) Alpha-particle spectrum measured in the 6th strip of SD for 300 s after the 30-s beam irradiation. The inset shows a decay curve of the 6.790-MeV α peak of ^{206}Fr measured in all the strips of SD. The beam intensity was 1.9 pμA. (c) Alpha-particle spectrum measured in the first top detector of the rotating wheel system MANON for 30 s after the 30-s aerosol collection. The beam intensity was 1.8 pμA. The helium flow rate was 5 L min^{-1} and the chamber pressure was 90 kPa. The temperature of the KCl aerosol generator was 620 °C.

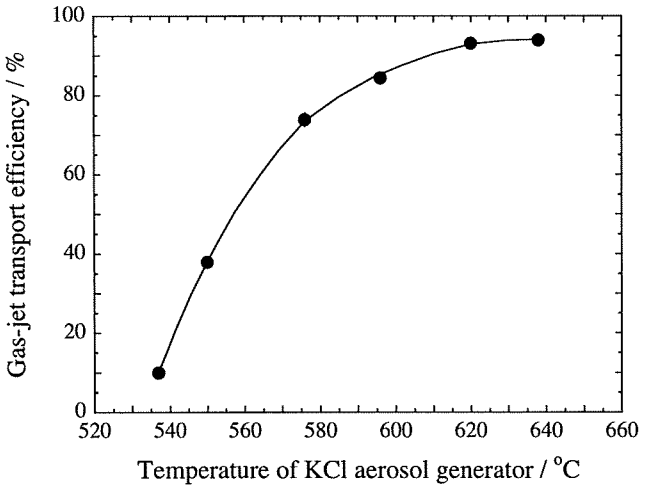

Figure 3. Variation of the gas-jet transport efficiency of ^{206}Fr as a function of the temperature of KCl aerosol generator. The helium flow rate was 5 L min^{-1} and the chamber pressure was 90 kPa. The ^{40}Ar beam intensity was 1.7 pμA.

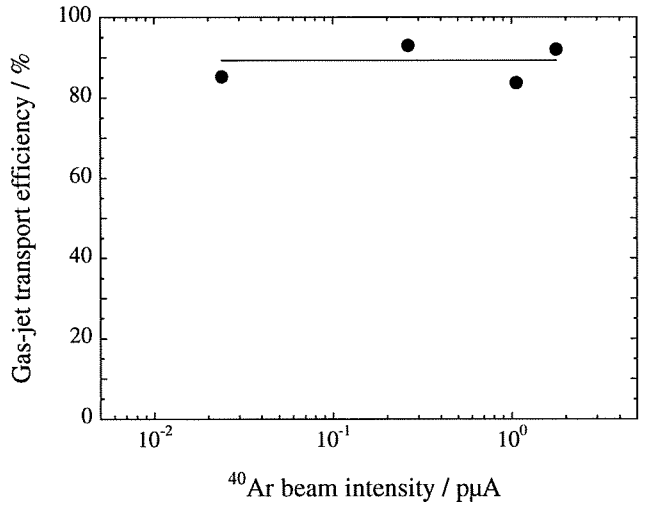

Figure 4. Variation of the gas-jet transport efficiency of ^{206}Fr as a function of the ^{40}Ar beam intensity. The helium flow rate was 5 L min^{-1} and the chamber pressure was 90 kPa. The temperature of the KCl aerosol generator was 620 °C.

the spectrum, indicating that the gas-jet transport of ^{206}Fr to MANON was successfully conducted after the physical separation by GARIS. The transport efficiency of the gas-jet system was evaluated using the 6.790-MeV α peak of ^{206}Fr.

In Figure 3, the gas-jet transport efficiencies of ^{206}Fr are shown as a function of the temperature of the KCl aerosol generator. The efficiency increases smoothly with an increase of the temperature and attain to over 90% at 620 °C. The variation of the gas-jet efficiencies of ^{206}Fr is shown in Figure 4 as a function of the ^{40}Ar beam intensity. The efficiencies are constant irrespectively of the beam intensities up to 2 pμA. In the conventional gas-jet system in that the beam passes through the target chamber, the gas-jet efficiency decreases due to the increasing plasma condition induced by the intense beam. As an example, we previously measured the gas-jet efficiencies of ^{173}W produced in the ^{nat}Gd(^{22}Ne,xn) reaction without the beam separation by GARIS. It was found that the gas-jet efficiency of ^{173}W drastically decreases from 40% at 6.6 pnA to 25% at 0.5 pμA with increasing beam intensity. Since the beam is separated by GARIS in the present experiment, such a decrease of the gas-jet efficiency is not observed for ^{206}Fr as shown in Figure 4.

Alpha-particle spectra of ^{245}Fm under the beam-on and beam-off conditions are shown in Figures 5(a) and 5(b), respectively. Although no α peaks are seen in the beam-on

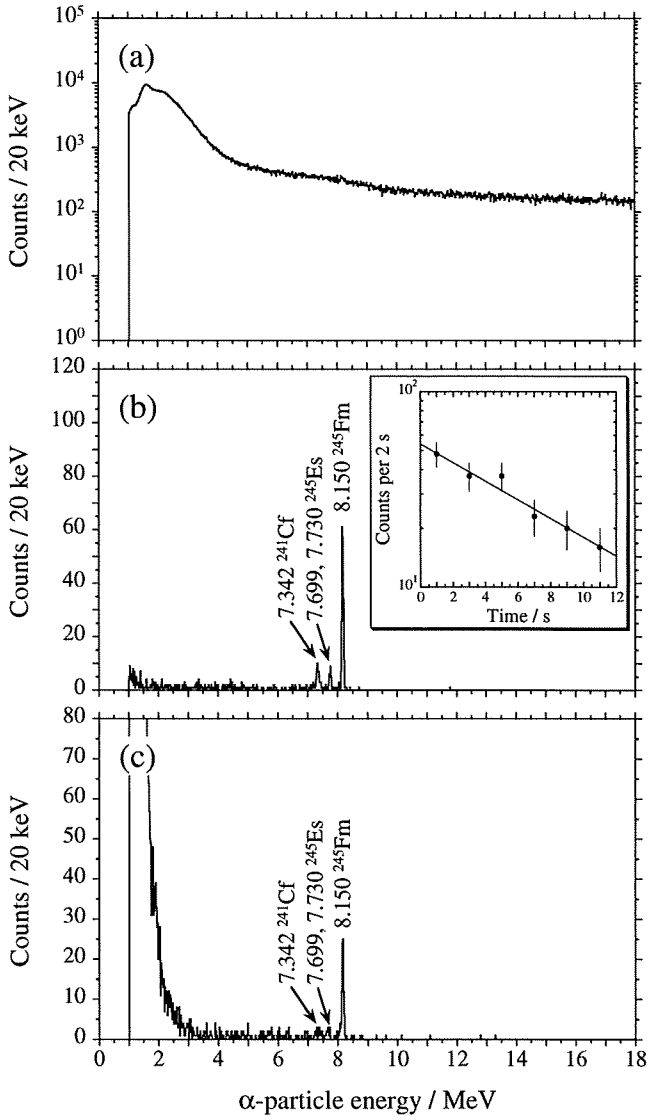

Figure 5. Sum of α-particle spectra measured in the ^{245}Fm experiment in the 12-strip Si detectors (SD) under (a) the beam-on and (b) beam-off conditions. The cycle of the beam-on (5 s) and beam-off (15 s) measurements was repeated 1265 times. The ^{40}Ar beam dose of 6.55 × 10^{16} was accumulated. The inset shows a decay curve of the 8.150-MeV α peak of ^{245}Fm. (c) Sum of α-particle spectra measured in the seven top detectors of the rotating wheel system MANON for 14 s after the 2-s aerosol collection. The 2-s aerosol collection was repeated 7289 times. The beam dose was 9.76 × 10^{16}. The helium flow rate was 5 L min^{-1} and the chamber pressure was 90 kPa. The temperature of the KCl aerosol generator was 620 °C.

spectrum (Figure 5(a)), α peaks of ^{245}Fm (4.2 s, 8.15 MeV)[17] and its daughter ^{241}Cf (3.78 min, 7.342 MeV)[17] are clearly seen in the beam-off spectrum (Figure 5(b)). The decay curve of the 8.15-MeV α peak is shown in the inset of Figure 5(b). The half-life of ^{245}Fm was determined to be 6.3 ± 1.3 s, which agrees with the literature value of 4.2 ± 1.3 s.[17] The α peaks around 7.7 MeV would be those of ^{245}Es (1.1 min, 7.699 and 7.730 MeV)[17] produced in the ^{208}Pb(^{40}Ar,p2n)^{245}Es reaction or the EC decay of ^{245}Fm. Background α-particles of, e.g., ^{211}Bi and ^{211m,212m}Po which are produced in the transfer reactions on the ^{208}Pb target[15] are completely removed by GARIS. The separation factors in excess of 10^4 were evaluated for ^{211}Bi and ^{211m,212m}Po based on their cross sections reported in Reference 15.

Compared in Figure 5(c) is the sum of α-particle spectra measured in the seven top detectors of MANON. The 8.15-MeV α peak of ^{245}Fm is clearly seen in the spectrum, and the gas-jet transport efficiency is determined to be 83 ± 9%. Despite of the physical separation by GARIS, one can see a lot of background events in Figure 5(c), especially below 4 MeV.

Since MANON was placed in the target room in this experiment, these background events were caused by large amounts of neutrons and/or γ rays during the irradiation. Very recently, we have constructed a chemistry laboratory isolated with a 50-cm concrete shield from the target room, where the background level is two orders of magnitude lower than that in the target room.

In this work, the high gas-jet efficiencies over 80% were obtained both for ^{206}Fr and ^{245}Fm. The recoil range of ^{206}Fr in helium at 90 k Pa is calculated to be 30 mm based on the SRIM 2006 code,[18] and that of ^{245}Fm is extrapolated to 18 mm from those of the lower Z ions (Z = 68–92) of A = 245. These recoil ranges are short enough as compared with the helium thickness of the gas-jet chamber used in this work (60 mm at 90 kPa). In the conventional gas-jet system in that the beam passes in the recoil chamber, the helium gas is swept out through the capillary outlet to the vertical direction of the beam axis. Therefore, the position of the capillary outlet in the chamber should be adjusted to the recoil ranges of the product nuclei of interest. Since the beam is separated by GARIS in the present system, we can put the capillary outlet at the center end of the chamber (see Figure 1(c)). Thus, helium gas is fed into the chamber through the four inlets directed to the surface of the Mylar window and is swept out thoroughly from the end of the chamber. In addition to the beam-free condition, this smooth helium flow in the chamber would be advantageous to the high gas-jet efficiency.

4. Summary and Perspectives

We have developed the gas-jet transport system coupled to GARIS as a preseparator for the SHE chemistry. The performance of the system was demonstrated using ^{206}Fr and ^{245}Fm produced in the ^{169}Tm(^{40}Ar,3n)^{206}Fr and ^{208}Pb(^{40}Ar,3n)^{245}Fm reactions, respectively. The α particles of ^{206}Fr and ^{245}Fm separated with GARIS and transported by the gas-jet were clearly observed with a rotating wheel system for α spectrometry. The high gas-jet efficiency of over 80% was found to be independent of the beam intensity up to 2 pμA. These results suggest that the GARIS/gas-jet system is a promising tool for future SHE chemistry at RIKEN. Recently, the gas-jet transport of ^{255}No produced in the ^{238}U(^{22}Ne,5n) reaction was also successful with the gas-jet efficiency over 80%. In the future, productions of SHE nuclides with long half-lives for chemical experiments such as ^{261}Rf, ^{262}Db, ^{265}Sg, ^{269}Hs, and ^{283}112 will be studied with the present system using ^{238}U and ^{248}Cm targets.

Acknowledgement. The authors express their gratitude to the crew of the RIKEN Linear Accelerator for their invaluable assistance in the course of these experiments. This research was partially supported by the REIMEI Research Resources of Japan Atomic Energy Research Institute, 2003, and by the Ministry of Education, Science, Sports and Culture, Grant-in-Aid for Young Scientists (B), 16750055, 2004–2006.

References

(1) *The Chemistry of Superheavy Elements*, Ed. M. Schädel, Kluwer Academic Publishers, Dordrecht (2003).
(2) M. Schädel, Angew. Chem. Int. Ed. **45**, 368 (2006).
(3) *6th Workshop on Recoil Separator for SHE Chemistry, Garching, Germany, September 29, 2006*: http://www-w2k.gsi.de/tasca06/.
(4) J. P. Omtvedt, J. Alstad, H. Breivik, J. E. Dyve, K. Eberhardt, C. M. Folden III, T. Ginter, K. E. Gregorich, E. A. Hult, M. Johansson, U. W. Kirbach, D. M. Lee, M. Mendel, A. Nähler, V. Ninov, L. A. Omtvedt, J. B. Partin, G. Skarnemark, L. Stavsetra, R. Sudowe, N. Wiehl, B. Wierczinski, P. A. Wilk, P. M. Zielinski, J. V. Kratz, N. Trautmann, H. Nitsche, and D. C. Hoffman, J. Nucl. Radiochem. Sci. **3**, 121 (2002).
(5) L. Stavsetra, K. E. Gregorich, J. Alstad, H. Breivik, K. Eberhardt, C. M. Folden III, T. N. Ginter, M. Johansson, U. W. Kirbach, D. M. Lee, M. Mendel, L. A. Omtvedt, J. B. Patin, G. Skarnemark, R. Sudowe, P. A. Wilk, P. M. Zielinski, H. Nitsche, D. C. Hoffman, and J. P. Omtvedt, Nucl. Instrum. Methods Phys. Res. A **543**, 509 (2005).
(6) Ch. E. Düllmann, G. K. Pang, C. M. Folden III, K. E. Gregorich, D. C. Hoffman, H. Nitsche, R. Sudowe, and P. M. Zielinski, *Advances in Nuclear and Radiochemistry, General and Interdisciplinary, Vol. 3*, Eds. S. M. Qaim and H. H. Coenen, Forschungszentrum Jülich GmbH, Jülich (2004), p 147.
(7) Ch. E. Düllmann, C. M. Folden III, K. E. Gregorich, D. C. Hoffman, D. Leitner, G. K. Pang, R. Sudowe, P. M. Zielinski, and H. Nitsche, Nucl. Instrum. Methods Phys. Res. A **551**, 528 (2005).
(8) R. Sudowe, M. G. Galvert, Ch. E. Düllmann, L. M. Farina, C. M. Folden III, K. E. Gregorich, S. E. H. Gallaher, D. C. Hoffman, S. L. Nelson, D. C. Phillips, J. M. Schwantes, R. E. Wilson, P. M. Zielinski, and H. Nitsche, Radiochim. Acta **94**, 123 (2006).
(9) U. W. Kirbach, C. M. Folden III, T. N. Ginter, K. E. Gregorich, D. M. Lee, V. Ninov, J. P. Omtvedt, J. B. Patin, N. K. Seward, D. A. Strellis, R. Sudowe, A. Türler, P. A. Wilk, P. M. Zielinski, D. C. Hoffman, and H. Nitsche, Nucl. Instrum. Methods Phys. Res. A **484**, 587 (2002).
(10) K. Morita, K. Morimoto, D. Kaji, H. Haba, E. Ideguchi, J. C. Peter, R. Kanungo, K. Katori, H. Koura, H. Kudo, T. Ohnishi, A. Ozawa, T. Suda, K. Sueki, I. Tanihata, H. Xu, A. V. Yeremin, A. Yoneda, A. Yoshida, Y.-L. Zhao, T. Zheng, S. Goto, and F. Tokanai, J. Phys. Soc. Jpn. **73**, 1738 (2004).
(11) K. Morita, K. Morimoto, D. Kaji, H. Haba, E. Ideguchi, R. Kanungo, K. Katori, H. Koura, H. Kudo, T. Ohnishi, A. Ozawa, T. Suda, K. Sueki, I. Tanihata, H. Xu, A. V. Yeremin, A. Yoneda, A. Yoshida, Y.-L. Zhao, and T. Zhen, Eur. Phys. J. A **21**, 257 (2004).
(12) K. Morita, K. Morimoto, D. Kaji, T. Akiyama, S. Goto, H. Haba, E. Ideguchi, K. Katori, H. Koura, H. Kudo, T. Ohnishi, A. Ozawa, T. Suda, K. Sueki, F. Tokanai, T. Yamaguchi, A. Yoneda, and A. Yoshida, J. Phys. Soc. Jpn. **76**, 043201 (2007).
(13) K. Morita, K. Morimoto, D. Kaji, T. Akiyama, S. Goto, H. Haba, E. Ideguchi, R. Kanungo, K. Katori, H. Koura, H. Kudo, T. Ohnishi, A. Ozawa, T. Suda, K. Sueki, H. Xu, T. Yamaguchi, A. Yoneda, A. Yoshida, and Y.-L. Zhao, J. Phys. Soc. Jpn. **73**, 2593 (2004).
(14) D. Vermeulen, H.-G. Clerc, C.-C. Sahm, K.-H. Schmidt, J. G. Keller, G. Münzenberg, and W. Reisdorf, Z. Phys. A **318**, 157 (1984).
(15) J. M. Nitschke, R. E. Leber, M. J. Nurmia, and A. Ghiorso, Nucl. Phys. **A313**, 236 (1979).
(16) Y. Nagame, M. Asai, H. Haba, S. Goto, K. Tsukada, I. Nishinaka, K. Nishio, S. Ichikawa, A. Toyoshima, K. Akiyama, H. Nakahara, M. Sakama, M. Schädel, J. V. Kratz, H. W. Gäggeler, and A. Türler, J. Nucl. Radiochem. Sci. **3**, 85 (2002).
(17) R. B. Firestone and V. S. Shirley, *Table of Isotopes, 8th ed.* John Wiley & Sons, New York (1996).
(18) J. F. Ziegler, *The Stopping and Range of Ions in Matter, SRIM*: http://www.srim.org/.

CdTeを用いたX線画像検出器モジュールの開発

（株）アクロラド
玉城　充　　三戸 美生　　首藤 靖浩
山口 浩司　　喜友名 達也　山本 雅也
寒河江 健一　喜名　徹

1．はじめに

従来、X線撮像装置として一般撮影などの静止画撮影においてはスクリーン-フィルムシステムや輝尽性蛍光体(イメージングプレートI.P)を用いたＣＲシステムが使用されてきたが、現像作業あるいはレーザー読出し作業が必要であるためリアルタイム性に欠けるといった面がある。また、フィルムの保管などの問題もある。一方、消化管系や血管造影などの透視撮影においてはイメージインテンシファイア(I.I)とＴＶカメラまたはＣＣＤカメラと組み合わせたＴＶ撮像システムが使用されてきたが、視野が円形であることや周囲部において画像の歪みが生じる。 またI.Ｉの電子レンズ部分は真空管で製作されているため装置の小型化には限界がある。このような背景のなか、近年フラットパネルディテクタ（Flat Panel Detector　以下 FPD）が登場し、既存のX線撮像装置で存在した問題が克服され、実際の臨床の現場で普及し始めている。特に従来では困難であった静止画撮影と透視撮影の両立が期待されている。またFPDの構造上、検出器部分の厚さを薄くできるために装置の小型化も容易になると思われる。

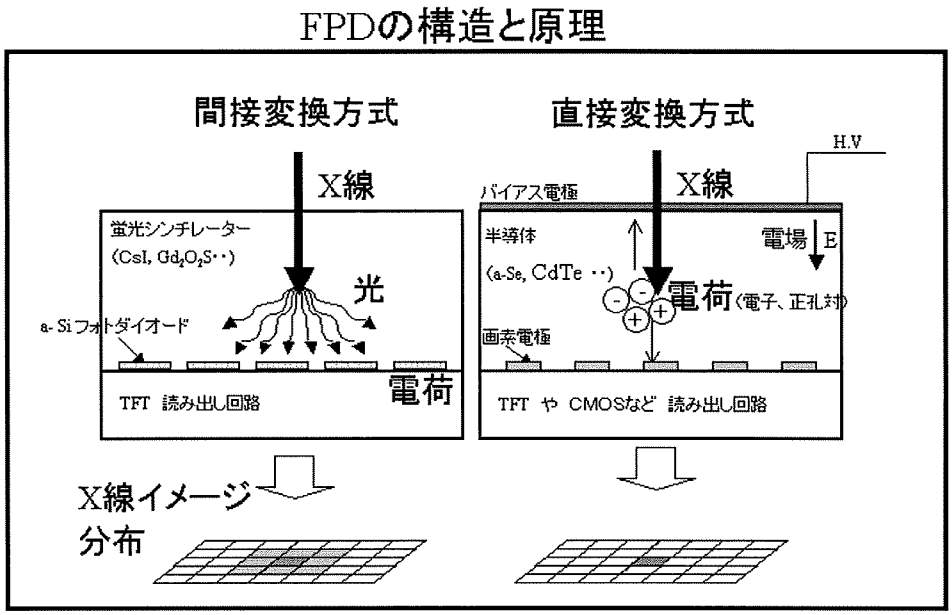

図１.FPDの構造と原理

現在、FPDと呼ばれるものは、入射X線を電荷に変換する原理の違いから間接変換方式と直接変換方式に大別される。図１にFPDの構造と原理を示す。間接変換方式の原理は、外部から入射す

るX線はCsIやGd_2O_2Sなどの蛍光シンチレーターによって一旦光に変換され、その後a-Siなどのフォトダイオードによって光から電荷に変換される。その後、蓄積された電荷はスイッチング機能を持つ薄膜トランジスタ(TFT)回路やCMOS回路などの読出し回路で信号として取り出される。この間接変換方式では原理上、シンチレーターの発光効率及びフォトダイオードの電荷変換効率による損失が起きるためX線検出感度に影響を及ぼす。また、シンチレーター内で光の散乱が起こるため、隣接ピクセルへの影響が避けられず、２次元画像上では、画像のボケが生じる。最近、シンチレーターを数μm径の柱状結晶にすることでボケを抑える工夫がされているが画素ピッチに相当する鮮鋭度は得ることは困難である。

一方、直接変換方式の原理は、入射したX線はアモルファスセレン(a-Se)やテルル化カドミウム(CdTe)などの半導体内で直接電荷に変換され、蓄積された電荷はTFTやCMOS回路で読み出される。この直接変換方式では最大の特徴は入射したX線は、直接電荷変化されるため極めて変換効率が良いこと、また半導体内には外部からの高電圧印加により高い電場が形成されており X線により生成された電子正孔対は直ちに対面電極へ収集されるため、ボケもなく鮮鋭度が非常に高いことである。このような背景から我々は、CdTe半導体を用いた直接変換方式のX線画像検出器モジュールを開発した。

2. CdTe半導体の特徴

CdTe 半導体の優れた特徴のひとつに原子番号と物質密度が比較的大きいために放射線に対する吸収効率が高いことが挙げられる。図２は単一エネルギー（80keV）を持つX線に対する吸収効率を示す。比較のために現在のFPDのX線変換部分に主に使用されているCsIシンチレーター、a-Se半導体も記載してある。厚さ1mmのCdTe半導体を用いた場合80keVのX線フォトンに対する吸収効率が80%以上であり、これはa-Se半導体の3～4mm厚にも相当する非常に高い検出効率であることがわかる。

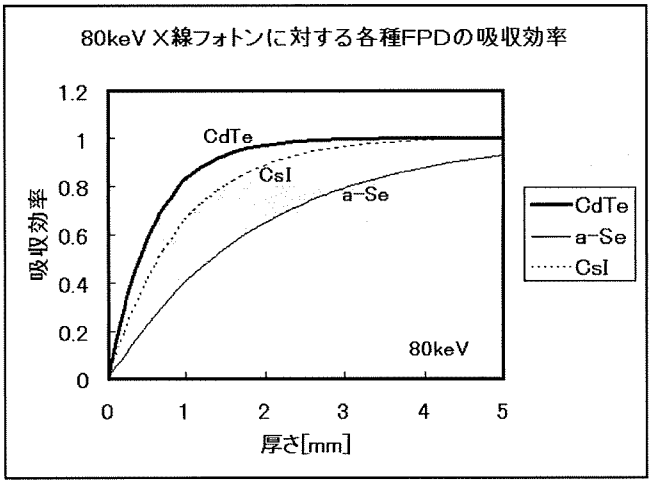

図２．80keVのＸ線に対する各種ＦＰＤの吸収効率